Bendable transparent films from cellulose nanocrystals–Study of surface and microstructure-property relationship

Carbohydrate Polymer Technologies and Applications 6 (2023) 100367

Contents lists available at ScienceDirect

Carbohydrate Polymer Technologies and Applications

journal homepage: www.sciencedirect.com/journal/carbohydrate-polymer-technologies-and-applications

Bendable transparent films from cellulose nanocrystals–Study of surface and microstructure-property relationship

Hannah Tideland [a], Jelka Feldhusen [b,c], Amit Kumar Sonker [b,c,d,*], Gunnar Westman [b,c,*]

[a] Department of Chemistry and Molecular Biology, University of Gothenburg, Gothenburg 40530, Sweden
[b] Department of Chemistry and Chemical Engineering, Chalmers University of Technology, Gothenburg 41296, Sweden
[c] Wallenberg Wood Science Center, Chalmers University of Technology, Gothenburg 41296, Sweden
[d] Cellulose films and coatings, Biomaterial Processing and Products, VTT Technical Research Centre of Finland Ltd. Tietotie 4E, Espoo 02150, Finland

ARTICLE INFO

Keywords:
Nanocellulose
Colloids and suspensions
Films
Sonication
Physiochemical properties

ABSTRACT

The presented work focuses on preparing transparent bendable films from nanocellulose. In comparison to cellulose nanofibrils and bacterial cellulose, nanocrystalline cellulose are shorter and have higher crystallinity (CI<95 %). Sulfated CNC (CNC_{IH}-OSO_3H) were prepared, and by changing their counter ions from H^+ to Na^+ and Et_4N^+ (Tetraethyl ammonium) flexible films were prepared with a strength of 70.5 MPa and 2.6 % elongation at break. The CNC suspensions showed excellent dispersibility in DI water with Zeta-potential (ζ) values > -35 mV. In the preparation of films, pre-sonication was key in improving the tensile strength and improved elongation (>30 % increase compared to films prepared without sonication) and hydrophobicity. The change of counter ion, H^+ to Na^+ or Et_4N^+, improved the thermal and mechanical properties of CNC films. The films were investigated with UV–Vis spectroscopy and optical polarized spectroscopy to explain the arrangement of nanocellulose crystals in correlation with the mechanical properties. The wettability of CNC samples was also studied and explained in detail. CNC from CelluForce was also studied as commercial reference samples. The modified CNC films have adequate properties for application in flexible electronics, energy storage, and biodegradable smart packaging.

1. Introduction

Cellulose nanocrystals (CNCs) are products of the most abundant polymer on earth and display remarkable mechanical and optical properties comparable to Kevlar and steel (Khattab et al., 2017; Moon et al., 2011; Norrrahim et al., 2021). Because of this, a great deal of effort has been put into transferring these nanoscale properties to macroscale materials. A key parameter in this is to develop methodologies for creating interphases that give the global structure flexibility, strength, and excellent optical properties such as transparency or uniform (tunable) structural color. Improvement of mechanical and optical properties of CNC-based films has generally focused on increasing the alignment of crystallites or tactoids in suspensions and, more recently, counteract effects such as capillary flow, which may distort the orientational order during drying. Methods to induce a large-scale linear (nematic) orientation across the film (ideally a nematic orientational order) include flow-based methods using a blade (Reising et al., 2012), confined shear (Jinkins et al., 2021), dip coating (Mendoza-Galván et al., 2019) and spin coating (Cranston & Gray, 2008), as well as magnetic (Revol et al., 1994; Sugiyama et al., 1992) and electric fields (Klockars et al., 2018; Tran et al., 2018). As can be expected, this linear nematic ordering has been shown to significantly improve the thermal, electrical, and mechanical properties in the longitudinal direction of CNC films (Reising et al., 2012) and CNC-based composites (He et al., 2014; Pullawan et al., 2012) at the expense of the same properties in the axial direction. This global anisotropy opens up applications where, e.g., the strength, flexibility, and conductivity in one direction is determinant for the performance of the device, e.g., in tissue engineering (He et al., 2014), optics (Wang et al., 2022), electronics (Csoka et al., 2012) and mechanical reinforcements in composites.

Above a critical volume fraction φ^* it becomes favorable for cellulose nanocrystals to self-assemble into cholesteric liquid crystals, beginning with small helically ordered droplets known as tactoids, which grow into larger cholesteric liquid crystalline structures as the volume fraction increases. In practice this concentration is commonly reported in critical weight fraction, c^*. Tactoids or cholesteric domains can also be oriented

* Corresponding authors at: Department of Chemistry and Chemical Engineering, Chalmers University of Technology, Gothenburg 41296 Sweden.
E-mail addresses: amit.sonker@vtt.fi (A.K. Sonker), westman@chalmers.se (G. Westman).

https://doi.org/10.1016/j.carpta.2023.100367

Available online 25 September 2023

in suspensions with concentrations above c^* with the help of magnetic (De France et al., 2016; Frka-Petesic et al., 2017; Kimura et al., 2005) and electric fields (Frka-Petesic et al., 2017; Kang & Eremin, 2021) circular shear (Park et al., 2014), vacuum-assisted self-assembly (after extensive sonication treatment) (Chen et al., 2014) and anchoring the helical axis orthogonally to the substrate (He et al., 2014; Pullawan et al., 2012), transforming the final films from a typical multi-domain structure, with multiple defects at boundaries between helicoidal domains where CNCs are poorly aligned, to a more uniform cholesteric order. This opens the door for high performance fracture-resistant biomimetic materials imitating the natural *Bouligand* structure (Natarajan & Gilman, 2018; Qin et al., 2019). Above c^* a high orientational order can also be achieved with relatively weak magnetic fields of 0.5–1.5 T (De France et al., 2016; Kimura et al., 2005; Revol et al., 1994) compared to the linear alignment of CNCs below c^* in μm-sized CNCs from tunicates where fields of 17.5, 20 T or higher have been found necessary (Frka-Petesic et al., 2019, 2015; Sugiyama et al., 1992). For some applications of thin films such as food packaging and protective coatings, the in-plane isotropic properties and fracture resistance that the cholesteric structure offers is preferable to macroscopic anisotropy, with the added benefit of uniform structural color, useful for applications such as sensors and coatings for anticounterfeiting (Eremeeva et al., 2020; Zhao et al., 2021), gas (Bardet et al., 2015; Dai et al., 2017) and humidity detection (Song et al., 2018; Zhao et al., 2021, 2019). However, processes during drying, including capillary flow, anchoring and other interactions with the substrate interfere with the uniformity of structure in both linear and cholesteric CNC films while vertical distortion of the helicoidal axis during drying reduces the uniformity of pitch in cholesteric CNC films (Frka-Petesic et al., 2019). A potential solution is to dry the CNC droplet under a layer of an immiscible liquid such as hexadecane. This was found to reduce capillary flow because water loss then happens uniformly across the suspension droplet, in addition to allowing more equilibration time (Zhao et al., 2019). Nevertheless, the pristine cholesteric structure is known to be brittle and have a high crack propensity. For example, in CNC/latex nanoparticle composites a highly uniform cholesteric structure exhibited ~50 % higher Young's modulus but ~73 % lower toughness than isotropic composites with the same composition (Vollick et al., 2017). In addition, the oil-covered droplets were only up to 1 mm in diameter and applying the same method to larger films, if possible, would be very time-consuming, which limits the range of applications. For suspensions which remain isotropic on the long range when kinetic arrest occurs the aggregation process during suspension drying is to the best of our knowledge not clearly understood and has garnered less attention in recent years. Instead, there has been advancement in controlling orientational order.

With the challenges above in mind, we looked at how physical methods, including sonication and drying conditions as well as chemical treatment, namely the replacement of the sulfate proton with a counter ion Na^+ or tetraethylammonium (Et_4N^+), affect large-angle, high-energy orientations between crystallites and defects on the micro and nanoscale in an attempt to improve elongation, tensile strength and reduce water permeability.

To optimize the preparation conditions, we investigated the influence of a 5 min ultrasound treatment ("sonication"), as well as three different drying conditions; ambient (room temperature, 40–70 % RH), 45 °C in a heating cabinet, and inside an evacuated desiccator, resulting in drying times of ~2–3, ~1 and ~7 days, respectively, on the mechanical properties and wettability for CNCs from two different sources with very different aggregation behavior.

Ultrasound treatment is widely reported to reduce the viscosity of CNC suspensions at moderate energy levels, reported at 5–40 kJ/g CNC (Beuguel et al., 2018; Dong et al., 1998; Gicquel et al., 2019; Shafiei--Sabet et al., 2012) thus prolonging the time until kinetic arrest is reached, mainly attributed to break-up of aggregates, which can give CNC films with lower optical haze and improved mechanical properties (Csiszar et al., 2016). It has also been reported to change the rheological behavior from a single shear-thinning region to the three-region behavior typical of a lyotropic liquid crystal (Shafiei-Sabet et al., 2012). Sonication and drying conditions of CNCs suspensions can drastically affect the onset and process of cholesteric liquid crystal self-assembly. The brief 5-min sonication and moderate energy level (222–485 J/mL suspension) here is based on five considerations: (i) long sonication hinders cholesteric phase formation; (ii) high sonication energies cause a deformation of crystallites and (iii) reduce the concentration for kinetic arrest, (iv) self-assembly is promoted by moderate sonication energies and (v) desulfation of sulfate half-ester groups should be minimized.

Longer evaporation time has been identified as beneficial for the uniformity of the cholesteric pitch because it results in fewer cholesteric domains that results in better alignment and consequently, CNC films with a more uniform *Bouligand*-like structure giving vivid structural colors (Klockars et al., 2018; Tran et al., 2018), as well as improved toughness, mainly due to crack deflection (Natarajan & Gilman, 2018b; Song et al., 2019; Yin et al., 2019). This appears to be a consequence of increased time for tactoids to relax into more energetically favorable orientations and fuse to form larger cholesteric domains at concentrations between c^* and kinetic arrest ("tactoid annealing") (Tran et al., 2018). Faster drying is therefore expected to reduce the time allowed for self-assembly. For long-rang isotropic suspensions faster drying could on the one hand lead to grain boundary strengthening, where a reduction in grain size in a certain size range, dependent on the particles, reduces the severity of defects, thus effectively improving the tensile strength (Ashby Michael & Jones David, 2012), while on the other hand equilibration of the crystalline structure is expected to be promoted by longer drying time and less thermal motion, at least during a critical stage before kinetic arrest

2. Materials and methods

2.1. Materials

Commercial samples of CNCs with sulfate half-ester surface groups (northern bleached softwood kraft pulp) with Na^+ as a counterions were purchased from CelluForce, Inc. (Montreal, Québec, Canada), in spray-dried form with a sulfur content of 0.89 wt.%, equivalent to 0.0462 OSO_3^- per anhydroglucose unit reported by the supplier. The CNC from Celluforce is called $SCNC_{CF}$ or CNC_{CF}-SO_3X, where X is H, Na^+ or Et_4N^+, when the details on the counter ion is discussed. The In-house CNC was prepared from microcrystalline cellulose (MCC) by sulfuric acid hydrolysis (Börjesson et al., 2018; Hasani et al., 2008) and is called $SCNC_{IH}$ and CNC_{IH}-SO_3X throughout the text. The expected size of CNC is 200 nm × 5–10 nm as per our previous work (Börjesson et al., 2018) The other chemicals, including Avicel PH-101 microcrystalline cellulose (cotton linters) with particle size (50 μm), HCl, NaOH and tetraethylammonium hydroxide (20 wt% in aqueous solution), $Et_4N^+OH^-$, were all purchased from Sigma Aldrich. Grade II de-ionized (DI) water was used for all dispersions and dilutions. All chemicals were used as delivered from the manufacturer without further purification.

The In-House batch of CNCs with sulfate half-ester groups grafted on the surface was prepared according to the procedure described by Hasani et al. (2008). Briefly, the aqueous $SCNC_{IH}$ or CNC_{IH}-OSO_3H suspension were prepared from MCC by sulfuric acid hydrolysis using 64 wt% sulfuric acid and continuously stirred at 45 °C for 2 h After hydrolysis, batches on a half kilogram scale where immediately dialyzed against deionized water until the effluent had a stable conductivity below 5 μS/cm. The SCNC particles were dispersed by sonication resulting in a stable colloidal suspension without any visible precipitate.

2.2. Methods

2.2.1. Preparation of suspensions of CNCs from Celluforce, CNC_{CF}-SO_3Na

The spray-dried CNC powder was resuspended in deionized water (typically 4–7 g CNC in 80–140 mL DI water) in a plastic vial (for >100 mL the amount was divided into two vials) and stirred for ~2 h to ensure uniform suspensions.

2.2.2. Characterization of suspensions

The concentration of the CNC batches of suspension was determined gravimetrically after drying three replicates of suspensions in polystyrene dishes (55 mm diameter) in hot air oven at 60 °C for 2 days, giving an average weight corresponding to 2.69 wt% of the total suspension (standard error of the mean 0.06 wt%).

2.2.3. Potentiometric and conductometric titration

Determination of sulfate (S) content was performed by conductometric and potentiometric titration of the extensively dialyzed suspension (conductivity <5 μS/cm in the surrounding water). 20 mL-samples of SCNC concentrations of 0.4 wt% were prepared in triplicates by adding, in the following order: NaCl solution (40 μmol, 0.5 M), deionized water and SCNC suspension. After vigorously shaking the resulting suspension was probe sonicated with an Ultrasonic Processor VC505 (20 kHz), during 1 min. The obtained sample was then titrated against NaOH (0.1 M solution) to determine the sulfate or sulfate half ester content on CNC_{IH}-OSO_3H samples with a Titrando 905 Metrohm, giving both conductometric and potentiometric titration in the same run. (See supplementary information for titration method, curves and calculations of sulfate content of sulfate half ester content). The surface sulfate half-ester concentrations (molality in μmol/g) reported here was calculated with the following formula:

$$[S]_{surf} = \frac{V_{NaOH}[NaOH]}{m_{CNC}} \quad (1)$$

where V_{NaOH} is the volume of added NaOH solution during the titration, [NaOH] is the concentration of NaOH solution (0.1 M) and m_{CNC} is the dry weight of SCNC in the titrated suspension.

2.2.4. Zeta-potential (ζ)

Zeta potential and hydrodynamic diameter measurements were performed on a Zetasizer Nano ZS (Malvern Instruments, Malvern, UK) using dynamic light scattering (DLS) (See details in supplementary information). The Smoluchowski approximation for larger particles with a relatively thin double layer was used to estimate zeta potential from electrophoretic mobility. A 50 mW diode-pumped solid-state laser was used as a light source. The scattering angle in DLS measurements was set to 173° Samples (10 mL) were prepared with 0.25 wt% SCNC, with and without additives in the same ratios as for the films, and with either no added electrolyte, or 20 μM or 1 mM NaCl solution (from 0.5 M stock solution). Complementary measurements adjusted the amount of NaCl to give a minimum conductivity of 300 μS/cm, meaning ~0.6 mM in the CNC_{IH}-SO_3H and ~1.3 mM in the CNC_{CF}-SO_3H sample. Samples were prepared by mixing 10 and 1 min of probe ultrasonication (sonication energy ~62 kJ/g SCNC) before transferal to transparent plastic disposable measurement cells from Malvern.

2.2.5. Preparation of films by solution casting method

Films of ~300 mg dry content were cast from CNC suspensions at room temperature on 55 mm diameter polystyrene dishes in H^+-and Na^+-counterion form with and without additives.

For $SCNC_{IH}$11.15 mL, 2.69 wt% CNC suspension were used whereas for $SCNC_{CF}$ 12 mL, 2.5 wt%, suspension where used. Na^+- and tetraethylammonium (Et_4N^+), samples were prepared in a molar ratio of 1:1 to the amount of surface half-ester (OSO_3H) groups by adding NaOH (0.176 mL 0.468 molal solution) and tetraethylammonium hydroxide (60.74 mg of 20 wt% solution) to aliquots of CNC.

From a suspension of $SCNC_{CF}$-SO_3Na from CelluForce, aliquots (12 mL CNC suspension) were used without further modification as well as with the addition of HCl (0.1 M stock solution) until a stable pH of ~3 had been reached.

In total, three different physical treatments were done before casting the films: (1) All samples were mixed for 15 min with a magnetic stirrer, (2) samples denoted Son were additionally treated with tip ultrasonication at 40 % power (Ultrasonic Processor VC505, 20 kHz) for 5 min and (3) samples denoted Son_{cold} were prepared in the same way as Son, but the sample vessel was also kept in an ice bath during sonication. The probe sonication instrument was allowed to cool for a minimum of 5 min between each sample and sonication energy varied between 11.1 and 18.3 kJ/(g SCNC) or 222 and 458 J/mL suspension. All modified films were prepared by applying the additive in the suspension before any mixing and sonication. The samples were then cast onto the petri dishes and left to dry either for several days in a fume hood at ambient conditions or ~24 h in a 45 °C oven, denoted 45 and Son-45 for suspensions that was sonicated), or for a week in an evacuated desiccator (denoted Vac and Son-Vac for suspensions that was sonicated).

2.2.6. Characterization of films

2.2.6.1. Surface functional groups – attenuated total reflectance-fourier transform infrared (ATR-FTIR) spectroscopy. FTIR spectra were obtained from a PerkinElmer FTIR Frontier Spectrum (PerkinElmer, Inc., Waltham, MA, USA) with a GladiATRM Single Reflection ATR (PIKE Technologies, Inc., Madison, WI) crystal. The samples were scanned in the frequency range 4000–400 cm^{-1} and collected at a resolution of 2 cm^{-1} with an average of 32 scans.

2.2.6.2. Mechanical properties of CNC films. Tensile testing was performed with an Instron Tensile Tester. The samples were prepared as per standard ASTM D882–12 in rectangular strips of dimension (4 cm x 1 cm) with 2 cm as gage length. The thickness of the strips was measured with a Mitutoyo micrometer by taking the average of three measurements in the region of the gauge length. Six replicates were measured for each type of film. The samples were stretched with strain rate of 2 mm/min.

2.2.6.3. X-ray diffraction (XRD) – crystallinity in CNC samples. X-Ray Diffraction (XRD) measurements were performed on a Bruker D8 Advance instrument in the range of 10–50° using scan rate 0.5 s/step using Cu K-a - 1.54 Å The samples were mounted on Silicon single crystal sample holder. The crystallinity Index of cellulose samples were measured by equation as described by Daicho et al. (2018)

$$CrystallinityIndex \quad (CI) = Area_{cryst}/Area_{Total} \times 100 \quad (2)$$

2.2.6.4. Thermal properties. Thermogravimetric analysis (TGA) was performed on a TGA/DSC 3 + Star system (Mettler Toledo, Switzerland). Samples were measured from the 30 to 500 °C temperature range using a heating rate of 10 °C/min. The first derivative of TGA, Differential Thermogravimetric analysis (DTGA), was also considered for determining decomposition stages in samples.

2.2.6.5. Polarized optical microscopy. Films were viewed with polarized optical microscopy (POM) using a CarlZeiss Axio Scope.A1 (Oberkochen, Germany) with linear polarizers at in a cross-polarizer setup in brightfield mode and magnification lenses 20x, 40x and 100x. Most micrographs were taken at the higher resolution. A droplet of CNC_{IH}-SO_3H-*Son* was also viewed while drying during ~1 h under crossed polarizers at 20x magnification. The droplet was applied on a glass slide cleaned with isopropanol and filmed for ~1 s in 1-min intervals. The film is in the Supplementary information.

2.2.6.6. UV-vis- light spectroscopy. UV-vis-light spectroscopy of solid films was performed on a PerkinElmer Lambda 950 UV-vis spectrophotometer, using air as a background from 300 to 800 nm wavelength. The central part of each film was placed in the upper part of the window in the sample holder at a 90° angle to the incident light. Replicates were taken of samples with visible variations in translucency and a sample corresponding to an intermediate value was selected for reporting the result. Attenuation coefficients were calculated from the Beer-Lambert law for a reflecting medium, assuming only one reflection at each interface and neglecting the imaginary part of the refractive index according to:

$$T = (1 - R)^2 \, e^{-\alpha d} \tag{3}$$

where T is the transmittance of light, $R = (n-1)/(n+1)^2$, n is the real part of the refractive index, α is the attenuation coefficient s and d is the thickness of the film. Attenuation coefficients α, were considered to account for both absorption and scattering. The Cauchy dispersion equation for refractive index (Jones et al., 2013) using the real part, with experimental constants reported by Niskanen et al. (2019) Eq. (3) for CNCs in the visible light range of 400–700 nm (in agreement with literary data Cranston & Gray, 2008; Landry et al., 2011; Reid et al., 2016) was applied and extrapolated to the interval 300–800 nm:

$$n_{eff} = 1.4767 + \frac{0.0063}{\lambda^2} - \frac{0.0002}{\lambda^4}. \tag{4}$$

The refractive indices were mainly intended to compare attenuation coefficients between films in this study and it is noted that values may vary slightly depending on the crystallinity of different CNC sources.

2.2.6.7. Wettability. The wettability of CNC films (IH or CF) was measured on the surface by contact angle measurements and the bulk through water absorption or swelling study. For surface wettability, contact angle measurements, optical goniometer was used from Attension. Bulk wettability was performed by immersing three pieces of CNC sample (each sample of 2 cm × 2 cm) in DI water in Petridish for 1 h. The absorbed water or swelling percentage was calculated using following equation.

Swelling percentage:

$$(S\%) = W_S - W_D/W_D \times 100, \tag{5}$$

where W_s and W_D are swollen weight and dry weight of CNC film samples

3. Results and discussion

3.1. Properties of cellulose nanocrystals (CNC) suspensions

Surface sulfate concentrations for $SCNC_{IH}$ and $SCNC_{CF}$ were 300 ± 25 μmol/g (Fig. S1 supplementary information) and 280 μmol/g, respectively. This is in the higher range typically reported for sulfated CNCs (Beck et al., 2015; Delepierre et al., 2021; Reid et al., 2017) as expected with the 2 h hydrolysis of CNC_{IH}-OSO_3H and extensive purification of CNC_{CF}-OSO_3Na in agreement with literature values of 250–330 μmol/g (Bertsch et al., 2019; Reid et al., 2017; Shafiei-Sabet et al., 2012).

All CNC samples show excellent dispersibility in DI water with ζ values>−30 mV and no significant difference was seen in zeta potential between suspensions of different counterions or sonicated versus non-sonicated suspensions (Table S1, Supplementary Information). However, dynamic light scattering (DLS) measurements indicate that $SCNC_{IH}$ suspensions had very large average hydrodynamic diameters of 6910 ± 983 and 8000 ± 1000 nm with H^+ and Na^+ counterions, respectively, which were reduced to 77 ± 2.31 nm and 89 ± 3.8 nm after sonication (De Souza Lima et al., 2003; Foster et al., 2018; Fraschini et al., 2014). A relatively high ionic strength (De Souza Lima et al., 2003; Foster et al., 2018; Fraschini et al., 2014) (1296 μS/cm for CNC_{IH}-OSO_3H) from the extensive hydrolysis and preparation conditions likely (De Souza Lima et al., 2003; Foster et al., 2018; Fraschini et al., 2014) promoted formation of larger clusters which was nevertheless broken up by the sonication treatment. While the large hydrodynamic diameter of suspensions without sonication is notable, all suspensions were stable without any visible sedimentation during storage over months (in line with the low ζ values), indicating the formation of lower-density clusters rather than dense aggregates. Lastly, (De Souza Lima et al., 2003; Foster et al., 2018; Fraschini et al., 2014) it should be noted that DLS is not strictly applicable to anisotropic particles (De Souza Lima et al., 2003), but still widely used in the literature for CNC suspensions as a semi-quantitative measure of particle size (Foster et al., 2018; Fraschini et al., 2014) and in this case as a proxy for aggregate/cluster size rather than individual SCNCs (Foster et al., 2018; Fraschini et al., 2014).

3.2. Surface functional groups on CNC – FTIR spectroscopy

Microcrystalline Cellulose (MCC) has its characteristic FTIR spectra (Aggarwal et al., 2023; Forsgren et al., 2019; Sonker et al., 2018; Sonker et al., 2016) with peaks at 3300–3400 cm-^{1} (for –OH hydroxyl groups), 2900 cm^{-1} (alkyl C—H stretching), 901 cm^{-1} (C-O-C bond between each glucose unit), 1640 cm^{-1} corresponds to absorbed water on the cellulose. It is observed that MCC and CNC samples have similar FTIR spectra full FTIR spectra, Fig. S2 in supplementary information) except for the formation of a new peak at 814 cm^{-1} corresponding to the C-O-S is observed on CNC surfaces due to the presence of sulfate half ester (Aggarwal et al., 2023) (Fig. 1). No change was observed in the peaks of CNC_{CF}-OSO_3H/Na and CNC_{IH}-OSO_3H/Na samples for region 814 cm^{-1}, whereas for CNC_{IH}-OSO_3Et_4N, there is a peak shift to 808 cm^{-1}.

3.3. Optical properties (Polarized optical microscopy and UV-Vis spectroscopy)

Polarized optical microscopy (POM), using cross-polarized light, as well as scanning electron microscopy (SEM) were used to gain understanding of the ordering on the microscale in the bulk of films parallel to the film surface as well as cross-sectionally, including the presence/absence of cholesteric structure, relative birefringence of and between films of similar thickness and the packing of grains/domains. This was complemented with UV/Vis-spectroscopy to identify cholesteric ordering through absorption peaks and overall light attenuation, indicative of scattering by voids or aggregates in films lacking cholesteric order and structural color.

Interference color ranges in each film were assessed in the software ImageJ by visual inspection of all POM micrographs (Figs. S5–S17). From the ubiquitous presence of interference colors, all SCNC films, regardless of source are seen to be birefringent except for a few small dark spots in otherwise uniformly colored $SCNC_{CF}$ films. A multi-domain structure is evident for $SCNC_{IH}$ and $SCNC_{CF}$-*Son* films from the significant variability in interference colors within and between samples of similar thickness. This is typical of CNC films produced by evaporation-assisted self-assembly where there is insufficient time for the structure to reach equilibrium before kinetic arrest as well as capillary flow and variability between interfacial and bulk drying conditions (Schütz et al., 2015, 2020). Rough estimates of birefringence and retardation wavelength were also made from an updated Michel-Lévy interference color chart (Sørensen, 2012) to get a comparison of the relative order between samples of different thickness (Tables S2 and S3). Since the chart only extends to samples of 50 μm thickness, while films were 58–115 μm thick, these values should not be taken as absolute. We do note that the chart has been used as an initial estimate of birefringence for significantly thicker CNC-based films of 600 μm on which more quantitative estimates can be made, e.g., with the help of UV–Vis reflectance (Kose et al., 2019). Upper estimates for thinner (average ≤70 μm) $SCNC_{IH}$ and $SCNC_{CF}$ films of 0.023 and 0.027 were also comparable to values

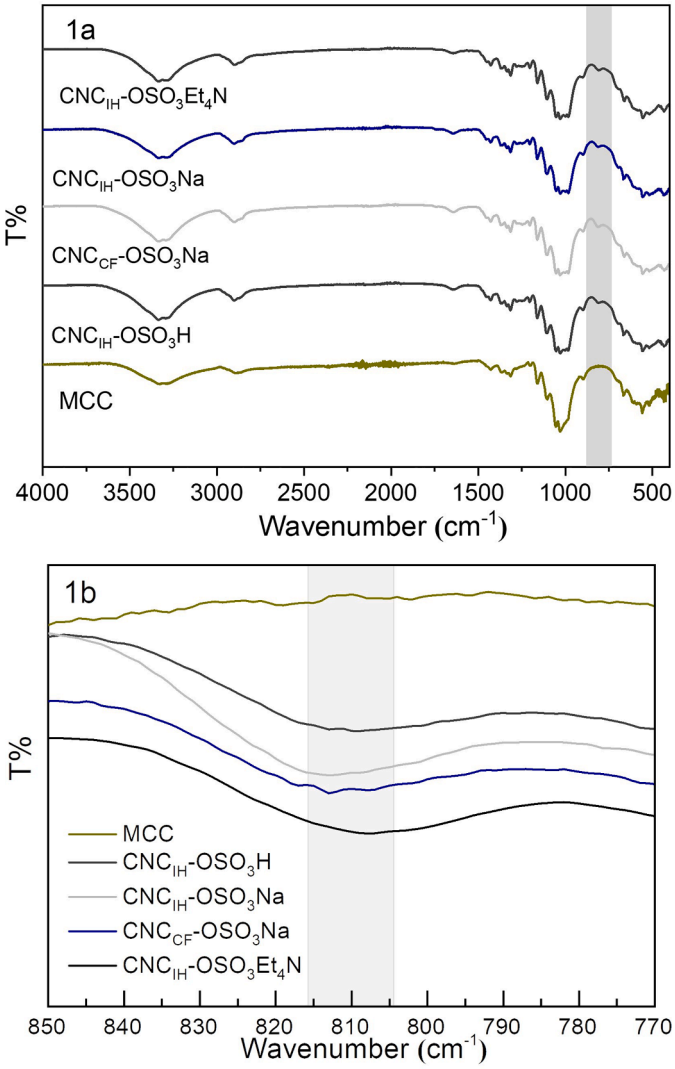

Fig. 1. (a) FTIR, full range (4000 – 400 cm^{-1}) (b) 850–770 cm^{-1} region of the FTIR spectra (Fig. S2 in supplementary information) indicates formation of sulfate half ester at 814 cm^{-1} after acid hydrolysis in CNC$_{CF}$-OSO$_3$H/Na and CNC$_{IH}$-OSO$_3$H/Na samples. A small shift of the characteristic sulfate ester group can be observed for the CNC$_{IH}$-OSO$_3$Et$_4$N sample from 814 to 808 cm^{-1}.

reported for very thin, linearly birefringent dip-coated CNC films, 0.021 and 0.026 for 2.8 and 6.0 μm thick films, respectively (Mendoza-Galván et al., 2019), as well as 0.0226 for linearly birefringent bacterial cellulose waveplates (De La Cruz et al., 2018), which is plausible for more highly ordered regions.

Based on suspension and film properties, including turbidity, apparent hydrodynamic diameter as well as transparency and microstructure seen in POM and SEM micrographs and UV/Vis spectroscopy we divide the films into three broad categories associated with different aggregation behavior during drying: (1) SCNC$_{IH}$ films (Fig. 2) from faster aggregating turbid suspensions, (2) slower aggregating SCNC$_{IH}$-*Son* (Fig. 3) and CNC$_{CF}$-OSO$_3$H films (Fig. 4a-d) from transparent suspensions forming near-transparent films without long-range order and (3) slower aggregating films displaying a multi-domain helicoidal long-range order from sonicated pristine CNC$_{CF}$-OSO$_3$Na suspensions (Fig. 4e-f).

SCNC$_{IH}$ films prepared without sonication (Fig. 2) all display a mosaic of grains with very small needle-shaped ~0.1–2 μm^2 cross-sections indicating that light is scattered and reflected in multiple directions. There are also multiple dark areas, especially in CNC$_{IH}$-OSO$_3$H, which, when zooming in and increasing the brightness, appear birefringent (Figs. S19 and S20), indicative of a void in the material rather than light extinction due to isotropy or the crystallites being oriented parallel to the viewing direction, which would result in light extinction regardless of brightness and magnification. This phenomenon is much less apparent after sonication and in SCNC$_{CF}$ films overall (Fig. 4). Sonicated SCNC$_{IH}$ films generally have much larger grains of similar interference colors with cross-sections of ~0.5–10 μm^2. This observation of difference in microstructure and hence scattering is supported by UV/Vis spectroscopy (Fig. 5) where light attenuation correlated strongly with the number and size of voids in the POM micrographs, with sonicated SCNC$_{IH}$ and SCNC$_{CF}$-OSO$_3$H films appearing nearly transparent and attenuating less than half the amount of light of films prepared without sonication at wavelengths above 325 nm (Fig. 5a and b). Films lacking fingerprint textures in the POM micrographs had a broad light attenuation, likely due to scattering, increasing towards the UV region, in agreement with the literature (Ling et al., 2020; Parit et al., 2018; Sirviö et al., 2016).

A porous structure along with higher turbidity of suspensions prepared without sonication suggests attractive driven cluster aggregation as the mechanism of liquid to solid transition (Cherhal et al., 2015), effectively resulting in kinetic arrest due to percolation, although confirming this requires nonlinear rheology tests and/or a small angle scattering technique such as SAXS. Nevertheless, large particles (indicated by the large hydrodynamic radii) would be expected to reach percolation at a lower concentration, allowing less time for relaxation into lower energy confirmations and providing a highly plausible explanation for the appearance of voids in the POM and SEM micrographs and lower transparency of films.

The more uniform microstructure, larger monochromatic birefringent areas, narrower birefringence range (Fig. S2), higher transparency, and fewer and smaller voids apparent in the SCNC$_{IH}$ Son films, Fig. 3, suggests that the break-up of aggregates with sonication leads to closer packing and improves the alignment of particles, likely because of slower aggregation (see discussion below). This effect was slightly less pronounced in the CNC$_{IH}$-OSO$_3$H-*Son* film with the lower 275 μmol/g CNC (Fig. 3a) but not 325 μmol/g CNC sulfur content (Fig. S7). This film which also had higher light attenuation than other -*Son* films (attenuation coefficient of 62.4 ± 11.9 cm^{-1} at 550 nm, Fig. 5, red), albeit with a significant reduction in apparent voids compared to films prepared without sonication, could be a consequence of accelerated acid-driven autocatalysis during sonication because of heat development (Beck & Bouchard, 2014; Jiang et al., 2010), resulting in an increase in the number of aggregates with sizes in the range of visible light. For neutral CNC$_{IH}$-OSO$_3$H (and the slightly basic CNC$_{IH}$-OSO$_3^-$Et$_4$N$^+$ suspensions) the desulfation at 5 min of sonication with a temperature of ~ 70 °C appears to be negligible (Beck & Bouchard, 2014). The effect was also, as expected, reduced when the suspension was cooled in ice bath during sonication, giving the overall lowest light attenuation (33.3 ± 0.6 cm^{-1} at 550 nm, Fig. 5) of SCNC$_{IH}$ films.

Interestingly, sonicated vacuum dried (Fig. 3h) and, to a lesser extent, 45 °C oven dried films from the same source and with the same counterion (Fig. 3d) also had larger monochromatic birefringent areas and almost as high transparency, despite no cooling (attenuation coefficients of 35.9 ± 2.8 cm^{-1} and 55.6 ± 2.5 cm^{-1} at 550 nm Fig. 5, magenta and blue). This may be a consequence of closer packing due to greater water loss, facilitating alignments between particles locally. However, the effect of 45 °C drying on light attenuation was generally small and a negative correlation was only observed in Change CNC$_{IH}$-OSO$_3$H-*Son-45* films. It is also notable that some fingerprint textures were visible in a drying CNC$_{IH}$-OSO$_3$H-*Son* sessile droplet on a glass slide (Supplementary Movie). Although the ordering is partly disrupted by radial capillary flow depositing and aligning particles along the edge, there is evidence that favorable substrate interactions facilitate self-assembly. Hydrophilic substrates have been found to give blue-colored self-assembled CNC films in contrast to hydrophobic substrates (including polystyrene), giving opaque films due to the tendency for

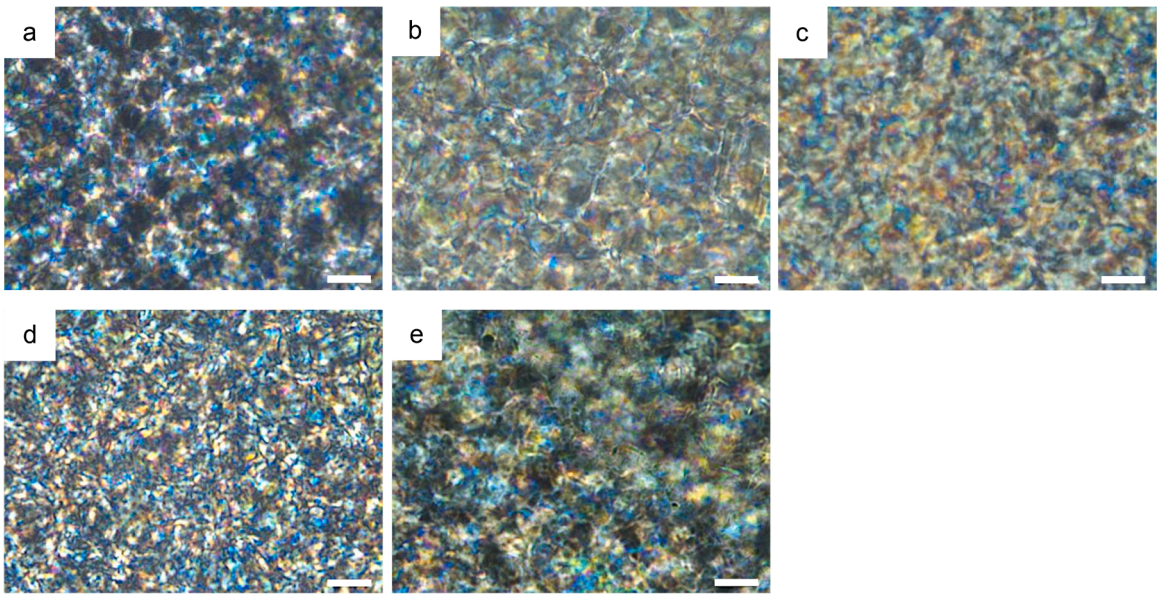

Fig. 2. POM micrographs of $SCNC_{IH}$ films prepared without sonication with counterions and conditions (a) H^+, (b) H^+ *45*, (c) H^+ *Vac*, (d) Na^+, (e) Na^+ *45*. The scale bars are 5 μm.

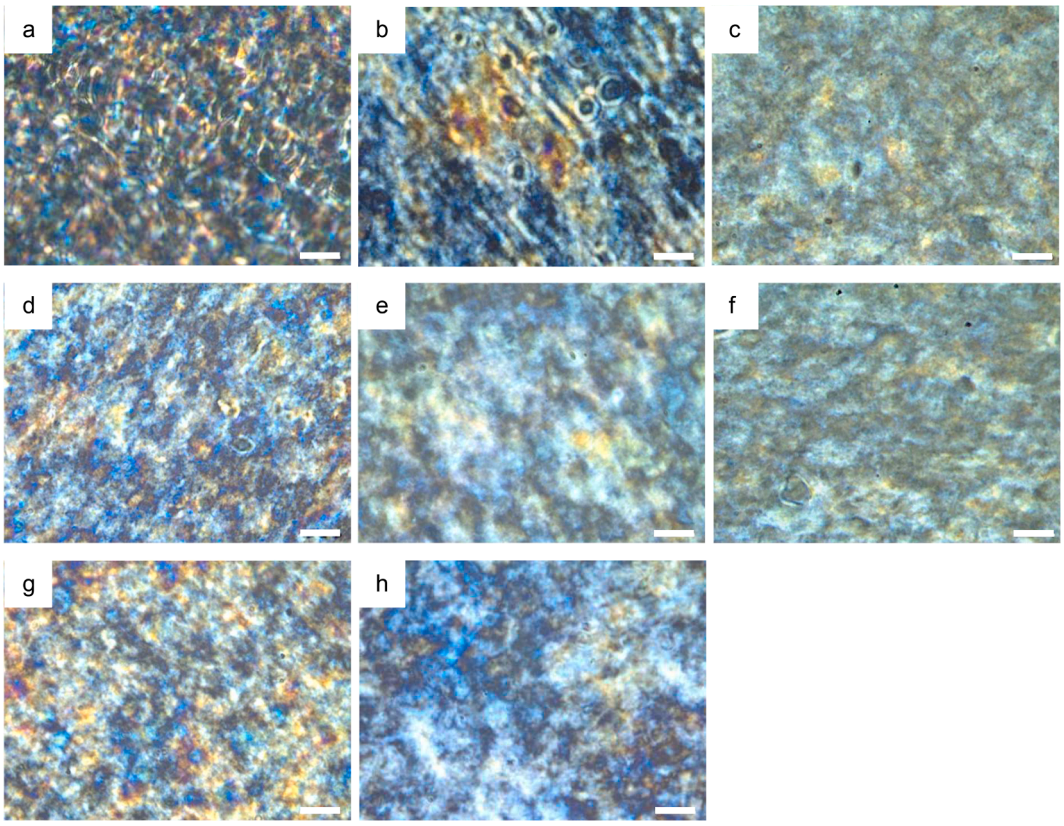

Fig. 3. POM micrographs of $SCNC_{IH}$-*Son* films with counterions and conditions (a) H^+ Son (b) Na^+-*Son*, (c) Et_4N^+-*Son*, (d) H^+-*Son-45*, (e) Na^+-*Son-45*, (f) Et_4N^+-*Son-45* (g) H^+-Son_{cold} (cooling in ice bath during sonication) and (h) H^+-*Son-Vac*. The scale bars are 5 μm.

suspensions to minimize contact with the substrate. In the same category, the non-iridescent $SCNC_{CF}$ films without fingerprint patterns, absorption peaks or a visible helical structure in SEM were overall the most transparent, particularly the CNC_{CF}-OSO_3H-*Son* samples (5, red line,8.5 $\pm$ 0.3 cm^{-1} at 550 nm). The higher transparency is likely a consequence of lower ionic strength in theses samples (vide infra) resulting in net attractive interactions at higher concentrations than in the $SCNC_{IH}$ suspensions.

Sonication of CNC_{CF}-OSO_3Na suspensions also resulted in a drastic change in film microstructure from birefringent with relatively uniform interference color across the film to having multiple helical domains from the dried and compressed cholesteric liquid crystal domains, as can be seen from the fingerprint lines of varying width and orientation in Fig. 4e-g and Figs. S16–S18 and a greater variation of birefringence

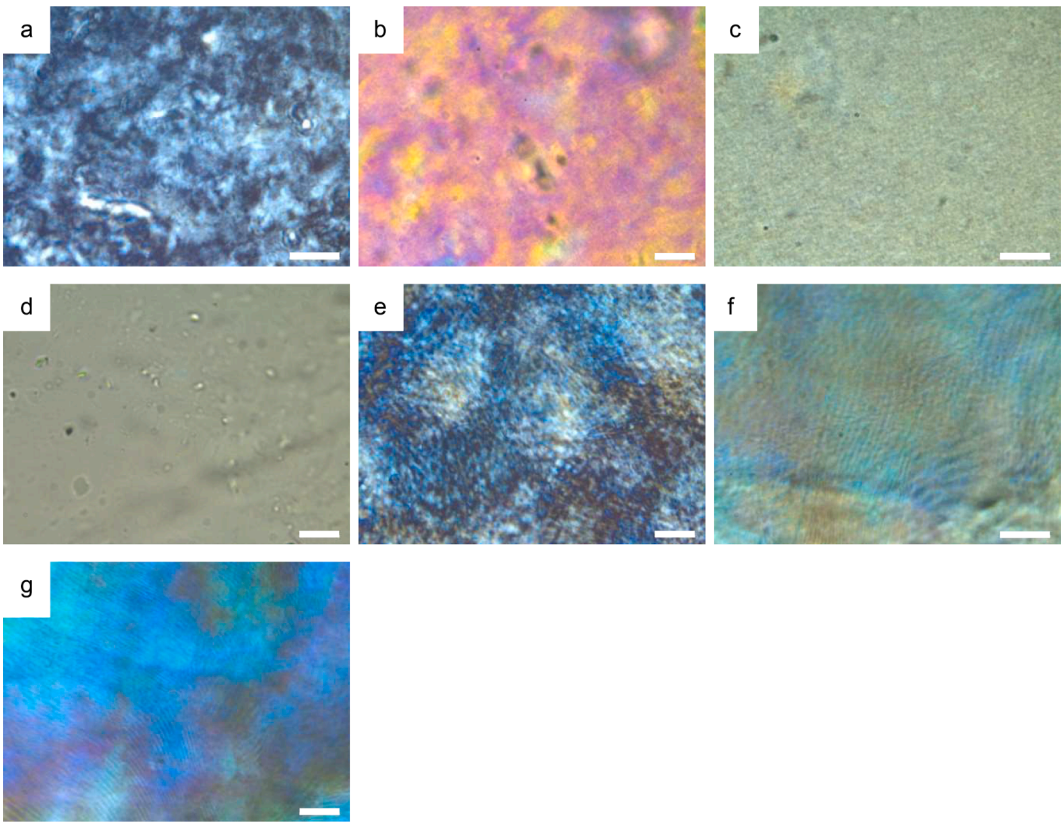

Fig. 4. POM micrographs of CNC_{CF}-OSO_3 films with (a) H^+, (b) Na^+, (c) Na^+ 45, (d) H^+-*Son*, (e) Na^+-*Son*, (f) Na^+-*Son-45* and (g) Na^+-*Son-Vac*. Note the fingerprint patterns in the sonicated Na^+ counterion films in e-f, indicative of cholesteric structure. The scale bars are 5 μm.

(Table S2). Fingerprint lines are visible where the axis of helical domains are oriented parallel or slightly tilted against the film surface with dark lines (Fig. 4e and g) corresponding to nematic planes where CNCs are oriented with the long axis perpendicular to the film plane (Roman & Gray, 2005), the increased drying time (~7 days instead of 2–3 days) of CNC_{CF}-OSO_3Na-*Son-Vac* suspensions resulted in larger helicoidal domains (see Fig. 4g), visibly lower pitch as indicated by the decreased width of fingerprint textures and peak absorption wavelength (Fig. 5d, magenta), in agreement with current literature (Chen et al., 2014; Klockars et al., 2018; Tran et al., 2018; Zhao et al., 2019). As expected, multi-domain structured films resulted from all drying conditions with 1½ to 7 days of drying time (it is reported to take from several days up to six months for the liquid crystalline structure to reach equilibrium (Schütz et al., 2015) and the uniformity of the dried structure is still counteracted by processes such as capillary flow and substrate interactions). The ambient, 45 °C dried, and vacuum-dried films had red, orange, and yellow structural colors in the center, respectively, corresponding to peak absorption wavelengths of 770, 620 and 574 nm (Fig. 5) and a red shift towards the edges. The absorption band of vacuum-dried films was narrower, indicative of a more uniform pitch and interestingly, also in 45 °C oven dried films (Fig. 5, blue and magenta). This is notable since the drying time was shorter, in contrast with what has been found to promote pitch uniformity (Klockars et al., 2018; Tran et al., 2018) and indicates that the loss of rotational and translational freedom of the CNCs with less bound water dominates over thermal motion at this temperature during evaporation.

The different microstructure between suspensions from CF and IH both with and without sonication can be attributed to differences in self-assembly and aggregation behavior mainly due to a significantly higher ionic strength of IH suspensions. This is indicated by a more than 6 times higher conductivity of 1296 μS/cm for CNC_{IH}-OSO_3H compared to 218 μS/cm for the CNC_{CF}-OSO_3Na suspension without sonication, which likely resulted from different hydrolysis and purification steps. However, the higher specific conductivity of $H+$ may slightly exacerbate the effect on conductivity compared to Na^+ ions (Conway, 1969). CNC_{IH}-OSO_3H was hydrolyzed for two hours while producing SCNCs by CelluForce only involves 25 min of hydrolysis (Hamad & Hu, 2010; Wang et al., 2016), as well as additional purification steps required to produce redispersable freeze-dried CNCs. We note that electrical conductivity generally increases with ionic strength, but the relationship is not straightforward for polyelectrolyte solutions at these concentrations unless the surface charge is effectively screened. In this case, a linear relationship has been observed for aqueous solutions of carboxymethylcellulose (Bordi & Cametti, 1986) and carboxymethyl dextran (Sagou et al., 2015). A higher ionic strength results in a shorter Debye screening length, κ^{-1}, which in this range likely gave a higher c^* (Abitbol et al., 2018; Dong et al., 1996; Honorato-Rios et al., 2016) and earlier onset of kinetic arrest for $SCNC_{IH}$ because attractive interactions would have started to dominate earlier as the ionic strength increased with evaporation (Honorato-Rios et al., 2018).

Depending on the balance of attractive and repulsive interactions, liquid-to-solid transitions (partly) disordered charged colloidal suspensions are commonly described in terms of gelation or an attractive or repulsive glass transition (Tanaka et al., 2004). Attractive Van der Waals interactions drive gelation. Repulsive glass is dominated by electrostatic repulsion, while in attractive glasses, the system is in attractive energy well on the order of the thermal energy, k_BT, where the particle concentration is high enough for electrostatic "jamming" to occur (Tanaka et al., 2004). The arrested dynamics also occur quite abruptly in glass transition at a specific volume fraction, while fractal gelation happens more gradually, starting at lower concentrations, with a power-law dependence on volume fraction (Solomon & Spicer, 2010). Longer and thinner rod particles tend to form both liquid crystalline and glassy states more readily (Solomon & Spicer, 2010). Despite the similar sulfate

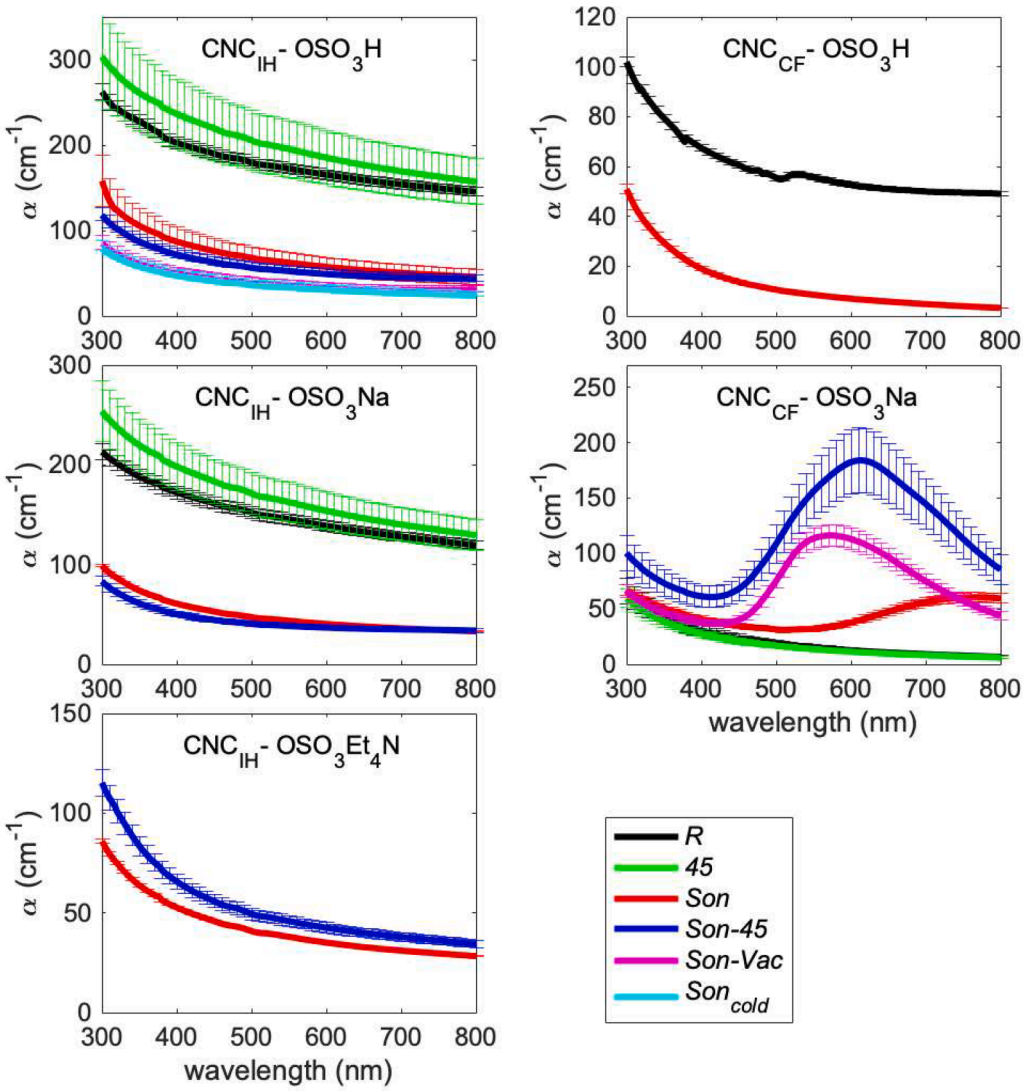

Fig. 5. Attenuation coefficients for films prepared under the following conditions: reference, no additional physical treatment (R, black), 45 °C drying in heating cabinet (*45*, green), sonication (*Son*, red), sonication and 45 °C drying (*Son-45*, blue), sonication and vacuum drying (*Son-Vac*, magenta) and sonication in ice bath (*Son$_{Cold}$*, cyan). Counterion, source and additive are indicated by the titles and legend. Attenuation coefficients were calculated assuming a refractive index varying according to (3). Error bars represent standard deviation.

contents, different aggregation behaviors are clearly apparent from the conductivity and turbidity of the suspensions before sonication and differing microstructure and light attenuation of films. This evidence points to significant contributions to ionic strength aside from the CNCs themselves in SCNC$_{IH}$ suspensions, most likely including harder bound ions and oligosaccharides remaining from the hydrolysis. The high opacity and conductivity of these suspensions without sonication indicates an attractive-driven (gel) liquid-to-solid transition (Oguzlu et al., 2017; Phan-Xuan et al., 2016; Xu et al., 2020, 2018). It should also be noted that CNC$_{CF}$ are produced from softwood and the CNC$_{IH}$ is prepared from MCC, cotton linters. This may give the crystallites variations, such as different shapes of cross-section or rotation of the C6 or other disorders that are neglected, or unknown.

An estimate of the mode of liquid to solid transition for the pristine CNC$_{CF}$-OSO$_3$Na suspension can be made based on phase diagrams by Xu et al., of added NaCl against CNC concentration (determined from nonlinear rheology tests of CNCs from the University of Maine Process Development Center (Xu et al., 2018) as well as multiple literary data (Xu et al., 2020)). The boundary point between viscoelastic fluid and attractive gel, attractive glass, and repulsive glass states is reported at ~15 mM added NaCl and a dimensionless concentration of ~0.8[74], corresponding to the product of volume fraction and aspect ratio. The sulfate content, aspect ratios, and added salt reported by the authors (Xu et al., 2018) correspond to an ionic strength of 24–51 mM (40 mM on average). With aspect ratios of 13–30.5 (Reid et al., 2017, Shafiei-Sabet et al., 2012), and a surface sulfate concentration of 300 μmol/g CNC, the same reasoning puts the ionic strength of CNC$_{CF}$-OSO$_3$Na at 13–30 mM. Without accounting for the possible effects of sonication on the onset of kinetic arrest, the SCNCs from CelluForce without added salt are likely to have undergone a repulsive glass transition. This is consistent with observations by Fazilati et al. (2021) of unexpected oscillations between shear stresses dominated by restructuring and destructuring in SCNC$_{CF}$, similar to observations of other soft glassy materials (Coussot et al., 2006; Fazilati et al., 2017; Tabuteau et al., 2007).

The cholesteric ordering of CNC$_{CF}$-OSO$_3$Na films after sonication can most likely be attributed to (i) a reduction in the number of irregularly shaped, larger aggregates, (ii) an increase in fully dispersed crystallites and smaller aggregates or "bundles" with high rectangularity (similar to individual crystallites), which have been suggested to act as chiral dopants (Parton et al., 2022) as well as a reduction in width polydispersity (Beck et al., 2015; Parton et al., 2022), and (iii) a reduction in viscosity widely reported with sonication (Coussot et al., 2006; Fazilati

et al., 2017; Tabuteau et al., 2007). These effects are consistent with a longer equilibration time of the cholesteric structure and supported by a study by Gicquel et al. (2019), finding a drastic reduction of the time of phase separation between isotropic and anisotropic (cholesteric) phases from 5 to 7 days to 20 h with sonication. Furthermore, non-sonicated SCNCs from CF have been reported to display elastically dominated ($G'>G''$) behavior at lower concentrations (≥4 wt% Browne et al., 2022; Ranjbar & Hatzikiriakos, 2020) than the concentration at which the suspension is considered fully anisotropic (6.5 and 6 wt% Grey, 2021; Wojno et al., 2022) for non-sonicated and lower energy (bath) sonicated suspensions). However, we note that accounts on the effect of sonication on c^* and kinetic arrest of specifically SCNCs from CF vary somewhat in the published literature and may reflect variations in storage and redispersion conditions as well as the CNC preparation by the manufacturer (see Supplementary information).

According to the measure of thermally dissipated energy per suspension volume (J/mL) advised (Parton et al., 2022) based on the consistency of hydrodynamic diameter measurements, our input energy of 222–458 J/(mL suspension), was between values found to break up most irregular shaped aggregates into individual CNCs and bundles (Parton et al., 2022). However, the sulfate content here was twice as high (300 ± 25 μmol/g compared to 150–155 μmol/g), which may have altered the distribution of particle sizes and shapes somewhat.

Sonication releases some of the bound ions and possibly small residues of oligosaccharides between previously aggregated crystallites and the electrical double layer, presumably contributing to the formation of large aggregates in the $SCNC_{IH}$ suspension in the first place. However, the liquid-to-solid transition during subsequent drying in the sonicated suspensions differs and seems especially beneficial for mechanical and optical properties of CNC films from high ionic strength suspensions such as $SCNC_{IH}$. A change in the distribution of counterions in CNC suspensions after sonication has been suggested (Beuguel et al., 2018), resulting in a thinner double layer and thus, a reduction in viscosity but with the more homogenous distribution of ions slowing the aggregation that occurs in the non-sonicated suspension. The drastic reduction in the number and size of voids, increase in the size of birefringent grains, and narrower birefringence range observed in POM micrographs across the $SCNC_{IH}$-*Son* films also point to a greater alignment and closer packing between crystallites and grains consistent with a delayed aggregation. Some fracture of crystallites may have also contributed to a reduction in aspect ratio and higher ionic strength in the CNC_{IH}—OSO_3H suspensions due to accelerated acid-catalyzed desulfation with higher temperature during sonication (Beck & Bouchard, 2014).

As with the microstructure of grains seen in POM, the most significant parameters affecting light attenuation were whether the films had been sonicated, and whether they displayed evidence of a dried cholesteric structure (including iridescence and fingerprint patterns discussed above). This can largely be attributed to differences in ionic strength and ion distribution affecting the liquid to solid transition kinetics, which determines the size and orientation of grains and voids in the final film. The added ionic strength from HCl disrupted cholesteric ordering, most likely because of faster liquid-to-solid transition in the more attractive-driven system but was sufficiently low to hinder the formation of larger voids and aggregates. In $SCNC_{CF}$ films, a weak negative correlation between attenuation coefficients and vacuum radii (but not hydrated radii) of counterions was also observed, with absorption coefficients of 62.4 ± 11.9, 43.7 ± 0.6 and 38.0 ± 0.5 cm^{-1} for H^+, Na^+ and Et_4N^+ S films respectively.

3.4. Wettability

Contact angle measurements (surface wettability) and swelling tests (bulk wettability or water absorption) (Table 1) in water show a decreased wettability of films from sonicated suspensions. For example, in report by Alimohammadzadeh et al. (Alimohammadzadeh et al., 2023), the pure CNC films prepared by dilution and dispersion show

Table 1
Swelling percentage, with maximum stability time in water in brackets, and contact angle for CNC films. (For contact angle images see Fig. S2 in supplementary information).

SCNC suspension	Swelling%	Contact angle
CNC_{CF}-OSO_3H	Unstable	60.5°
CNC_{CF}-OSO_3H-*Son*	200 % (1 h)	86.1°
CNC_{CF}-OSO_3Na	Unstable	42.3°
CNC_{CF}-OSO_3Na-*Son*	190 % (5 min)	63.2°
CNC_{IH}-OSO_3H	Unstable	62°
CNC_{IH}-OSO_3H-*Son*	190 % (5 min)	72°
CNC_{IH}-OSO_3Na	Unstable	48°
CNC_{IH}-OSO_3Na-*Son*	175 % (5 min)	70°
CNC_{IH}-OSO_3Et_4N-*Son*	Unstable	72°
CNC_{IH}-OSO_3Na-*Son-45*	200 % (5 min)	69°
CNC_{IH}-OSO_3Na-*Son-Vac*	180 % (5 min)	75°

contact angle of 39° and it is comparable to CNC film used in our study prepared by mixing and dispersion. Further, higher wettability is obtained from the same suspension by sonication (Table 1). Also, the effect of counter-ion was also observed on wettability. CNC Films with H^+ counterions were more water resistant than those with Na^+. This could result from a greater inter-crystallite distance because of the larger hydrated radius of Na^+ ions (358 Å vs 280 Å (Nightingale, 1959; Volkov et al., 1997)) and H^+ counterions tending to give stronger and shorter inter-crystallite hydrogen bonds. While the hydrated radius is clearly diminished in a dried film, it is known that a significant amount of bound water remains at the interface between crystallites in dried CNC materials (Beck et al., 2011; Garg et al., 2020; Jiang et al., 2016; Natarajan et al., 2017) and the amount is likely to correlate with the fully hydrated size of the counterion.

Swelling and contact angles were similar for CNC films from both sources with the same counterion and with or without sonication. All films prepared without sonication were unstable in water and could not be recovered after a brief immersion. For $SCNC_{IH}$ films, this is likely related to the appearance of voids with cross-sections of hundreds of nanometers to micrometers seen in POM (Fig. 2). Larger voids likely formed as a result of the faster aggregation, compared to the greater orientation and closer packing in sonicated suspensions, but while voids provide space where water can diffuse, we expect that H^+-form of SCNC films have stronger interparticle hydrogen bonding than for other monovalent counterions, based on additional hydrogen bond donors from the OSO_3H groups being available. This is in line with previous findings for suspensions (Dong & Gray, 1997), freeze-dried CNCs (Beck et al., 2012), and spin-coated films (Liu et al., 2018) and might explain the lower apparent capacity of H^+ counterion films to swell in water before breaking apart beyond recovery. While the microstructure of $SCNC_{CF}$ films appears to be more uniform, the inability to recover them after water immersion indicates a greater disorder on the microscale in the polycrystalline film (but not on the scale of individual crystallites; all films had crystallinity indices above 95 % and no difference was seen with sonication, see Table 2), making hydrophilic crystallite faces more susceptible to uncontrollable absorption of water.

The CNC_{IH}-OSO_3Et_4N-*Son* film was also unstable in water, despite the sonication treatment, indicating that the larger counterion made the bulk structure more susceptible to the diffusion of water by increasing the inter-crystallite distance to the extent that water could quickly destabilize inter-CNC hydrogen bonds and Van-der-Waals interactions. On the other hand, the film has a slightly higher contact angle than the other -*Son* films of 75°, which is likely a consequence of a slightly more hydrophobic surface imparted by the ethyl groups.

All SCNC films with H^+ and Na^+ counterions swelled 175–200 % in water, with a maximum stability time of 5 min, except for CNC_{CF}-OSO_3H-*Son,* which was stable in the water much longer, up to 1 h. This film also had a significantly higher water contact angle, close to 90°, indicating a high hydrophobicity of the film surface and bulk despite no surface modification with hydrophobic groups. Instead, the

Table 2
Mechanical properties including tensile strength, σ, elongation at break, ε and crystallinity index, *CI*, for SCNC films.

SCNC film	σ (MPa)	ε (%)	*CI* (%)
CNC_{CF}-OSO_3H	39.7 (3.1)	1.9 (0.6)	95.6
CNC_{CF}-OSO_3H *Son*	54.6 (2.8)	2.4 (0.2)	96.2
CNC_{CF}-OSO_3Na	41.6 (3.3)	2.7 (0.5)	96
CNC_{CF}-OSO_3Na *Son*	65.4 (4.1)	2.1 (0.5)	96.5
CNC_{IH}-OSO_3H	28.2 (2.8)	1 (0.1)	96.2
CNC_{IH}-OSO_3H *Son*	65 (3.5)	2.8 (0.2)	97
CNC_{IH}-OSO_{3Na}	39.6 (3.8)	1.6 (0.1)	96.7
CNC_{IH}-OSO_3 *Son*	59.8 (3)	2.2 (0.5)	97
CNC_{IH}-OSO_3Et_4N *Son*	70.5 (3.7)	2.5 (0.6)	96.8
CNC_{CF}-OSO_3Na *Son-45*	63.25 (4)	1.5 (0.9)	95
CNC_{CF}-OSO_3Na *Son-Vac*	77.6 (3.8)	1.7 (0.4)	97
CNC_{IH}-OSO_3Na *Son-45*	61.4 (3)	2.2 (0.5)	97.5
CNC_{IH}-OSO_3Na *Son-Vac*	70 (4.1)	2.3 (0.8)	97.9

hydrophobicity is likely imparted by a very efficient packing, allowing many strong hydrogen bonds to form between crystallites and effectively excluding large amounts of water from diffusing between crystallites and out-competing the inter-crystallite hydrogen bonds. The swelling process is depicted in Fig. 6. When immersed in water, the film absorbed water quickly for the first 5 min, then gradually absorbed less until reaching saturation around the 60-min mark. After that, the film became unstable and gradually broke into smaller pieces, losing absorbed water.

3.5. Mechanical properties

The impact of counterion change on SCNC samples and processing parameters was also studied regarding the mechanical properties of films prepared from CNC suspensions (Fig. 7). Tensile strength (MPa) and elongation at break (%), along with crystallinity index, CI, are summarized in Table 2. The elastic modulus values for CNC_{IH} and CNC_{CF} samples are mentioned in the supplementary information (Table S5). The reliability of the modulus value is expected to be lower than ideal as the gage length of the sample used is only 2 cm, compared to the required gauge length of 10 cm in the standard used for tensile testing (ASTM-D88–12). Therefore, for CNC samples, values for elastic modulus are only considered to compare the difference between the type of samples and the effect of processing conditions like sonication and drying used to prepare the films. Sonication drastically improved the tensile strength, σ, in agreement with previous results for dry films from isotropic suspensions prepared with sonication treatment with similar energy (Csiszar et al., 2016). We find tensile strengths for all SCNC films

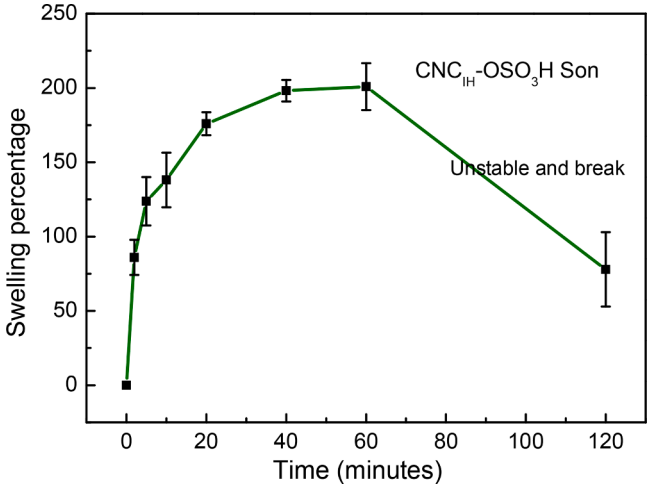

Fig. 6. Swelling behavior of the most water-resistant CNC_{CF}-OSO_3H S film as a function of time.

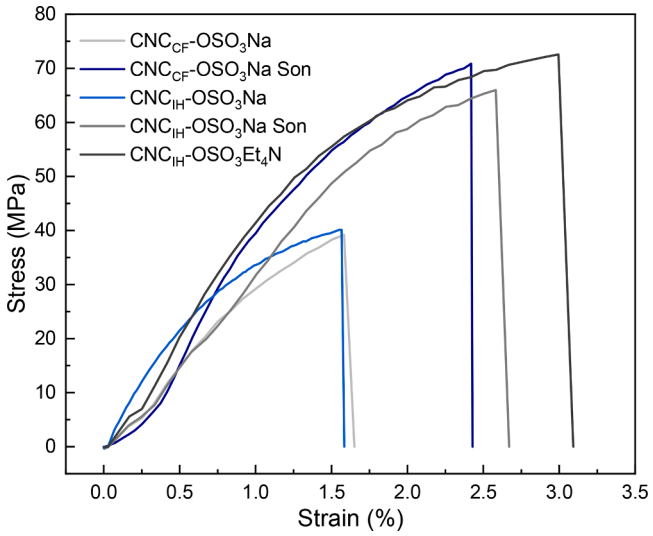

Fig. 7. Typical Stress-Strain diagram for CNC_{IH} and CNC_{CF} samples.

produced from sonicated suspensions (47–77 MPa) regardless of source, additives, counterions or whether cholesteric self-assembly occurred comparable to values reported for aligned free-standing CNC-based films discussed in the literature (Reising et al., 2012). This can be identified as a result of reduced defects and increased packing fraction.

A slightly higher elongation at break is also observed for films from both sources lacking long-range helical order dried in ambient conditions. Pristine helically structured CNC_{CF}-OSO_3Na-*Son* films had a higher stiffness (5.5–7.6 GPa compared to 4.0–5.5 GPa) but slightly lower elongation, in agreement with results for CNC-latex nanocomposites, which showed helically structured films to be more brittle, while isotropic films were more flexible (Vollick et al., 2017).

Films with Na^+ counterions were generally more flexible than with H^+ (except for CNC_{CF}-OSO_3Na*Son* films, likely due to the helical order). This may be an effect of a larger partly hydrated ionic radius in the dried films (see the discussion on wettability above). Furthermore, we found that the addition of a mole equivalent of the small, flexible, hydrophilic salt tetraethylammonium hydroxide (Et_4N^+OH), where Et_4N^+replaces H^+ as a counterion coordinating to the surface sulfate ester groups ($-OSO_3^-$), results in even higher elongation, because of stronger and more flexible intermolecular hydrogen bonding. Given the difficulty of using brittle materials, this suggests that for non-photonic applications and when flexibility is favored over stiffness, high-performance materials with local but not long-range order may be produced by relatively simple means.

Together with UV/Vis-light transmittance and POM results, tensile tests indicate that sonication leads to more efficient packing as water evaporates and the film assembles into a polycrystal solid, while lower humidity conditions during evaporation, including vacuum drying and drying in a heating cabinet at 45 °C, increases Young's modulus and reduces the elongation at break, ε. Note that the relatively flat microstructure with only few dark spots indicative of smaller voids and non-birefringent impurities for CNC_{CF}-OSO_3Na films (Fig. 4b and c) did not correlate with a higher tensile strength compared to CNC_{IH}-OSO_3Na S, indicating that grain boundary strengthening may be at least partly responsible for reduction of defects in long-range isotropic CNC films. Overall, σ and ε appear to improve up to a point where films and suspensions are transparent and display a uniform POM microstructure, particularly lacking any visible voids or mosaic structure indicative of larger disordered aggregates scattering in multiple directions. However, the mechanical performance does not scale directly with the optical properties. Further investigations of the structure-property relation from nano-to micro- and macroscale are warranted for long-range isotropic films, e.g., with SEM imaging of film cross-sections. Drying at 45 °C and

under vacuum resulted in a significantly lower elongation at break (but higher Young's modulus, see Supplementary information, Table S5). Since results were within standard error for both drying methods, the most likely explanation is the lower humidity conditions, leading to loss of bound water at crystallite interfaces. While the dependence on relative humidity makes water a problematic plasticizer for some applications, most bound water is generally stable in environments with slight humidity variation, e.g., electronic or optical applications, making the loss of plasticity from 45 °C unnecessary and unfavorable in many cases.

There are recent available reports in the literature, where CNC were reinforced with additives like Epoxy (Xu et al., 2022), Zinc oxide (Lizundia et al., 2016), Sodium alginate (Cai et al., 2020), proteins (Bast et al., 2021) to improve mechanical properties of CNC. In comparison to the published reports, tensile strength and elongation percentage break values are higher and comparable to the published reports. However, the comparison is not fair, as specimen size, standard of tensile test and testing conditions are different and that is possible reason for the variation observed in the mechanical properties of presented work and the published report.

3.6. Thermal properties

In addition to mechanical properties, the thermal properties of $SCNC_{CF}$ and $SCNC_{IH}$ films were studied to see the effect of counterion type on thermal stability. To highlight the difference in decomposition temperatures between the samples, the first derivative of the TGA plot was used as a differential thermal analysis (DTGA) (Fig. 8). The decomposition temperature is reduced from 338 °C in MCC to 174 °C in CNC_{IH}-OSO_3H films. The thermal stability is reduced because of the introduction of sulfate ester groups (C-O-SO_3H) that promote auto-catalyzed desulfation, which is faster at higher temperatures (Beck & Bouchard, 2014), followed by loss of water and de-polymerization (Kaur et al., 1987; Scheirs et al., 2001). The neutral and slightly basic SCNCs with Na^+ and Et_4N^+ counterions degrade more slowly, with

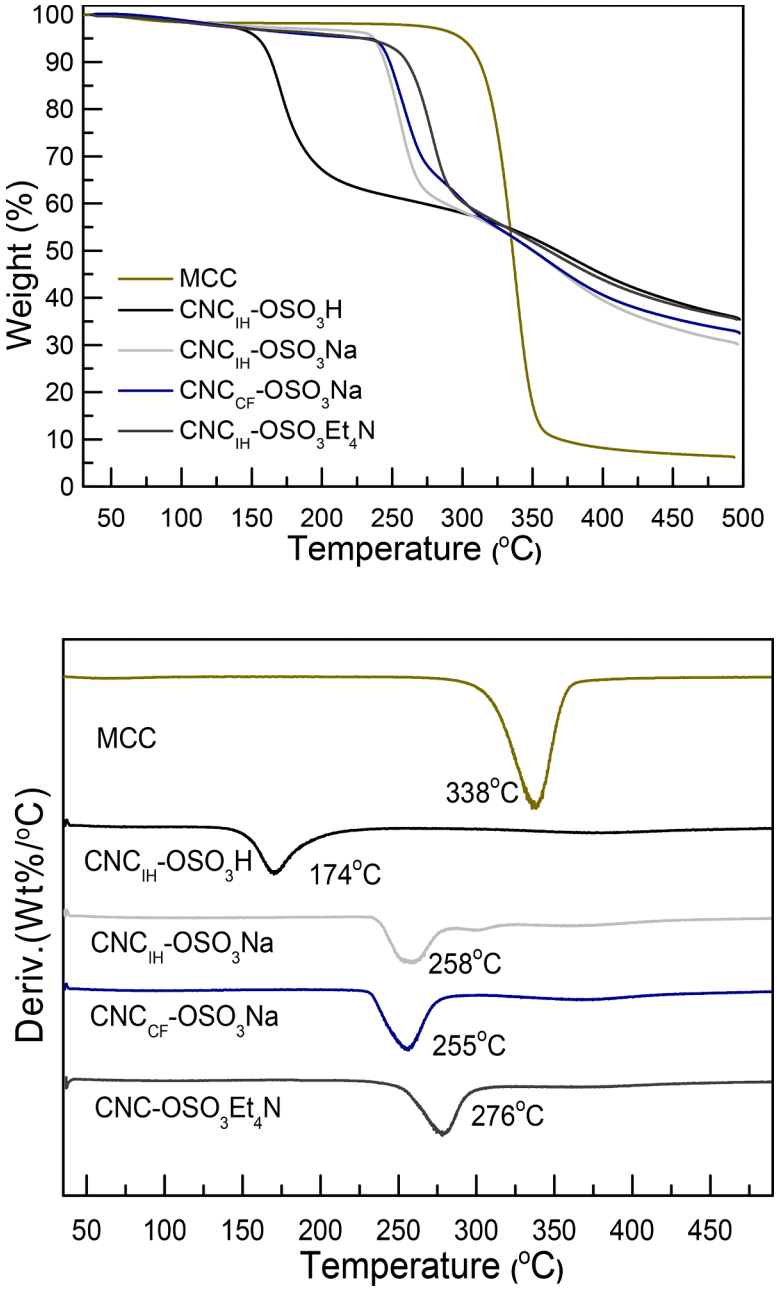

Fig. 8. TGA and DTGA spectra of MCC and different CNC films.

255–278 °C decomposition temperatures. This is expected since the first step of auto-desulfation is inhibited, in agreement with the literature (D'Acierno et al., 2020; Vanderfleet et al., 2019).

On comparing, the thermal stabilities of both the CNC from CelluForce and In-house, it is observed that CNC from CelluForce has higher thermal stability than the In-house CNC. It can be explained as the difference in sulfate content between them and source of cellulose from these are derived. With Cellulforce, the sulfate content is 250 μmol/g and for Inhouse CNC it is 300 μmol/g. Depending on the degree of sulfation, thermal stability of CNC samples also changes, and it is well described in the report by Lin et al. (Lin & Dufresne, 2014) In addition to sulfate content, thermal stability depends on kind of crystallinity of the source, dissociation constant of the reactant used, reactant concentration, reaction temperature, reaction time, evaporation rate, and post-treatment presence. For example, Cellulforce CNC is prepared from birch and Inhouse CNC are prepared from cotton linters and they show difference in the thermal stability (D'Acierno et al., 2023).

4. Conclusions

Films from sonicated suspensions from both in-house-made SCNCs and commercially produced SCNCs from CelluForce had significantly higher elongation at break, tensile strength, transparency, and greater water resistance on the surface and in bulk. Through polarized optical microscopy, this was identified due to the breaking up of larger aggregates that had contributed to scattering and inefficient packing. The dispersion of aggregates with sonication appears to be stable despite a high ionic strength of in-house SCNCs favoring attractive interactions and affecting the liquid-to-solid transition in favor of more efficient packing, typical of slower aggregating systems.

By varying parameters that can be efficiently and cost-effectively controlled, also on a large scale, namely drying conditions, sonication treatment, and counterions, we developed a facile procedure that gives comparable 2D-isotropic mechanical, thermal, and water-permeability properties to highly oriented films regardless of whether the films show a cholesteric structure or not. Therefore, we avoid the need for careful control of delicate factors such as polydispersity and crystallite length. Strong, tough, humidity and thermally resistant sulfated CNC (SCNC) films may serve as a starting point for various applications from composites to flexible electronics and smart food packaging.

Supplementary information

Characterization of different CNC samples by titration, FTIR, XRD, Crystallinity calculations, Zeta-potential, wettability (contact angle images), and polarized optical microscopy, tensile testing are explained in detail in the supplementary information.

Declaration of Competing Interest

The authors declare that they have no known competing financial interests or personal relationships that could have appeared to influence the work reported in this paper.

Data availability

Data will be made available on request.

Acknowledgment

AKS and GW thank Wallenberg Wood Science Center (WWSC) for financial support.

Supplementary materials

Supplementary material associated with this article can be found, in the online version, at doi:10.1016/j.carpta.2023.100367.

References

Abitbol, T., Kam, D., Levi-Kalisman, Y., Gray, D. G., & Shoseyov, O. (2018). Surface charge influence on the phase separation and viscosity of cellulose nanocrystals. *Langmuir: The ACS Journal of Surfaces and Colloids, 34*(13), 3925–3933.

Aggarwal, R., Garg, A. K., Saini, D., Sonkar, S. K., Sonker, A. K., & Westman, G. (2023). Cellulose nanocrystals derived from microcrystalline cellulose for selective removal of janus green azo dye. *Industrial & Engineering Chemistry Research, 62*(1), 649–659.

Ashby Michael, F., & Jones David, R. H. (2012). *10.7.1 grain-boundary strengthening (Hall-petch effect)*. Elsevier.

Bardet, R., Belgacem, N., & Bras, J. (2015). Flexibility and color monitoring of cellulose nanocrystal iridescent solid films using anionic or neutral polymers. *ACS Applied Materials & Interfaces, 7*(7), 4010–4018.

Bast, L. K., Klockars, K. W., Greca, L. G., Rojas, O. J., Tardy, B. L., & Bruns, N. (2021). Infiltration of proteins in cholesteric cellulose structures. *Biomacromolecules, 22*(5), 2067–2080.

Beck, S., & Bouchard, J. (2014). Auto-catalyzed acidic desulfation of cellulose nanocrystals. *Nordic Pulp & Paper Research Journal, 29*(1), 6–14.

Beck, S., Bouchard, J., & Berry, R. (2011). Controlling the reflection wavelength of iridescent solid films of nanocrystalline cellulose. *Biomacromolecules, 12*(1), 167–172.

Beck, S., Bouchard, J., & Berry, R. (2012). Dispersibility in water of dried nanocrystalline cellulose. *Biomacromolecules, 13*(5), 1486–1494.

Beck, S., Méthot, M., & Bouchard, J. (2015). General procedure for determining cellulose nanocrystal sulfate half-ester content by conductometric titration. *Cellulose (London, England), 22*(1), 101–116.

Bertsch, P., Sánchez-Ferrer, A., Bagnani, M., Isabettini, S., Kohlbrecher, J., Mezzenga, R., et al. (2019). Ion-induced formation of nanocrystalline cellulose colloidal glasses containing nematic domains. *Langmuir: The ACS Journal of Surfaces and Colloids, 35*(11), 4117–4124.

Beuguel, Q., Tavares, J. R., Carreau, P. J., & Heuzey, M. C. (2018). Ultrasonication of spray- and freeze-dried cellulose nanocrystals in water. *Journal of Colloid and Interface Science, 516*, 23–33.

Bordi, F., & Cametti, C. (1986). Equivalent conductivity of carboxymethylcellulose aqueous solutions with divalent counterions. *The Journal of Physical Chemistry, 90*(13), 3034–3038.

Börjesson, M., Sahlin, K., Bernin, D., & Westman, G. (2018). Increased thermal stability of nanocellulose composites by functionalization of the sulfate groups on cellulose nanocrystals with azetidinium ions. *Journal of Applied Polymer Science, 135*(10), 45963.

Browne, C., Raghuwanshi, V. S., Lin, M., Garnier, G., & Batchelor, W. (2022). Characterisation of cellulose nanocrystals by rheology and small angle X-ray scattering (SAXS). *Colloids and Surfaces A: Physicochemical and Engineering Aspects, 651*, Article 129532.

Cai, C., Wei, Z., Huang, Y., Wang, P., Song, J., Deng, L., et al. (2020). Bioinspired structure-robust cellulose nanocrystal films with enhanced water resistance, photothermal conversion ability, and fluorescence. *Cellulose (London, England), 27*(17), 10241–10257.

Chen, Q., Liu, P., Nan, F., Zhou, L., & Zhang, J. (2014). Tuning the iridescence of chiral nematic cellulose nanocrystal films with a vacuum-assisted self-assembly technique. *Biomacromolecules, 15*(11), 4343–4350.

Cherhal, F., Cousin, F., & Capron, I. (2015). Influence of charge density and ionic strength on the aggregation process of cellulose nanocrystals in aqueous suspension, as revealed by small-angle neutron scattering. *Langmuir: The ACS Journal of Surfaces and Colloids, 31*(20), 5596–5602.

Conway, B. E. (1969). *Electrochemical data. /* by B. E. Conway: Westport, Conn.: Greenwood Press.

Coussot, P., Tabuteau, H., Chateau, X., Tocquer, L., & Ovarlez, G. (2006). Aging and solid or liquid behavior in pastes. *Journal of Rheology, 50*(6), 975–994.

Cranston, E. D., & Gray, D. G. (2008). Birefringence in spin-coated films containing cellulose nanocrystals. *Colloids and Surfaces A: Physicochemical and Engineering Aspects, 325*(1–2), 44–51.

Csiszar, E., Kalic, P., Kobol, A., & Ferreira, E.d. P. (2016). The effect of low frequency ultrasound on the production and properties of nanocrystalline cellulose suspensions and films. *Ultrasonics Sonochemistry, 31*, 473–480.

Csoka, L., Hoeger, I. C., Rojas, O. J., Peszlen, I., Pawlak, J. J., & Peralta, P. N. (2012). Piezoelectric effect of cellulose nanocrystals thin films. *ACS Macro Letters, 1*(7), 867–870.

D'Acierno, F., Hamad, W. Y., Michal, C. A., & MacLachlan, M. J. (2020). Thermal degradation of cellulose filaments and nanocrystals. *Biomacromolecules, 21*(8), 3374–3386.

D'Acierno, F., Michal, C. A., & MacLachlan, M. J. (2023). Thermal stability of cellulose nanomaterials. *Chemical Reviews, 123*(11), 7295–7325.

Dai, S., Prempeh, N., Liu, D., Fan, Y., Gu, M., & Chang, Y. (2017). Cholesteric film of Cu (II)-doped cellulose nanocrystals for colorimetric sensing of ammonia gas. *Carbohydrate Polymers, 174*, 531–539.

Daicho, K., Saito, T., Fujisawa, S., & Isogai, A. (2018). The crystallinity of nanocellulose: Dispersion-induced disordering of the grain boundary in biologically structured cellulose. *ACS Applied Nano Materials, 1*(10), 5774–5785.

De France, K. J., Yager, K. G., Hoare, T., & Cranston, E. D. (2016). Cooperative ordering and kinetics of cellulose nanocrystal alignment in a magnetic field. *Langmuir: The ACS Journal of Surfaces and Colloids, 32*(30), 7564–7571.
De La Cruz, J. A., Liu, Q., Senyuk, B., Frazier, A. W., Peddireddy, K., & Smalyukh, I. I. (2018). Cellulose-based reflective liquid crystal films as optical filters and solar gain regulators. *ACS photonics, 5*(6), 2468–2477.
De Souza Lima, M. M., Wong, J. T., Paillet, M., Borsali, R., & Pecora, R. (2003). Translational and rotational dynamics of rodlike cellulose whiskers. *Langmuir: The ACS Journal of Surfaces and Colloids, 19*(1), 24–29.
Delepierre, G., Vanderfleet, O. M., Niinivaara, E., Zakani, B., & Cranston, E. D. (2021). Benchmarking cellulose nanocrystals part II: New industrially produced materials. *Langmuir: The ACS Journal of Surfaces and Colloids, 37*(28), 8393–8409.
Dong, X. M., & Gray, D. G. (1997). Effect of counterions on ordered phase formation in suspensions of charged rodlike cellulose crystallites. *Langmuir: The ACS Journal of Surfaces and Colloids, 13*(8), 2404–2409.
Dong, X. M., Kimura, T., Revol, J. F., & Gray, D. G. (1996). Effects of ionic strength on the isotropic−chiral nematic phase transition of suspensions of cellulose crystallites. *Langmuir: The ACS Journal of Surfaces and Colloids, 12*(8), 2076–2082.
Dong, X. M., Revol, J. F., & Gray, D. G. (1998). Effect of microcrystallite preparation conditions on the formation of colloid crystals of cellulose. *Cellulose (London, England), 5*(1), 19–32.
Eremeeva, E., Sergeeva, E., Neterebskaia, V., Morozova, S., Kolchanov, D., Morozov, M., et al. (2020). Printing of colorful cellulose nanocrystalline patterns visible in linearly polarized light. *ACS Applied Materials & Interfaces, 12*(40), 45145–45154.
Fazilati, M., Ingelsten, S., Wojno, S., Nypelö, T., & Kádár, R. (2021). Thixotropy of cellulose nanocrystal suspensions. *Journal of Rheology, 65*(5), 1035–1052.
Fazilati, M., Maleki-Jirsaraei, N., Rouhani, S., & Bonn, D. (2017). Quasi-periodic and irregular motion of a solid sphere falling through a thixotropic yield-stress fluid. *Applied Physics Express, 10*(11), Article 117301.
Forsgren, L., Sahlin-Sjövold, K., Venkatesh, A., Thunberg, J., Kádár, R., Boldizar, A., et al. (2019). Composites with surface-grafted cellulose nanocrystals (CNC). *Journal of Materials Science, 54*(4), 3009–3022.
Foster, E. J., Moon, R. J., Agarwal, U. P., Bortner, M. J., Bras, J., Camarero-Espinosa, S., et al. (2018). Current characterization methods for cellulose nanomaterials. *Chemical Society Reviews, 47*(8), 2609–2679.
Fraschini, C., Chauve, G., Berre, J. F., Ellis, S., Méthot, M., O'Connor, B., et al. (2014). Critical discussion of light scattering and microscopy techniques for CNC particle sizing. *Nordic Pulp and Paper Research Journal, 29*, 31.
Frka-Petesic, B., Guidetti, G., Kamita, G., & Vignolini, S. (2017). Controlling the photonic properties of cholesteric cellulose nanocrystal films with magnets. *Advanced Materials, 29*(32), Article 1701469.
Frka-Petesic, B., Kamita, G., Guidetti, G., & Vignolini, S. (2019). Angular optical response of cellulose nanocrystal films explained by the distortion of the arrested suspension upon drying. *Physical Review Materials, 3*(4), Article 045601.
Frka-Petesic, B., Radavidson, H., Jean, B., & Heux, L. (2017). Dynamically controlled iridescence of cholesteric cellulose nanocrystal suspensions using electric fields. *Advanced Materials, 29*(11), Article 1606208.
Frka-Petesic, B., Sugiyama, J., Kimura, S., Chanzy, H., & Maret, G. (2015). Negative diamagnetic anisotropy and birefringence of cellulose nanocrystals. *Macromolecules, 48*(24), 8844–8857.
Garg, M., Linares, M., & Zozoulenko, I. (2020). Theoretical rationalization of self-assembly of cellulose nanocrystals: Effect of surface modifications and counterions. *Biomacromolecules, 21*(8), 3069–3080.
Gicquel, E., Bras, J., Rey, C., Putaux, J. L., Pignon, F., Jean, B., et al. (2019). Impact of sonication on the rheological and colloidal properties of highly concentrated cellulose nanocrystal suspensions. *Cellulose (London, England), 26*(13), 7619–7634.
Grey, P. (2021). Cellulose nanocrystal chiral structures for electronics and photonics.
Hamad, W. Y., & Hu, T. Q. (2010). Structure–process–yield interrelations in nanocrystalline cellulose extraction. *The Canadian Journal of Chemical Engineering, 88*(3), 392–402.
Hasani, M., Cranston, E. D., Westman, G., & Gray, D. G. (2008). Cationic surface functionalization of cellulose nanocrystals. *Soft Matter, 4*(11), 2238–2244.
He, X., Xiao, Q., Lu, C., Wang, Y., Zhang, X., Zhao, J., et al. (2014). Uniaxially aligned electrospun all-cellulose nanocomposite nanofibers reinforced with cellulose nanocrystals: Scaffold for tissue engineering. *Biomacromolecules, 15*(2), 618–627.
Honorato-Rios, C., Kuhnhold, A., Bruckner, J. R., Dannert, R., Schilling, T., & Lagerwall, J. P. F. (2016). Equilibrium liquid crystal phase diagrams and detection of kinetic arrest in cellulose nanocrystal suspensions. *Frontiers in Materials, 3*.
Honorato-Rios, C., Lehr, C., Schütz, C., Sanctuary, R., Osipov, M. A., Baller, J., et al. (2018). Fractionation of cellulose nanocrystals: Enhancing liquid crystal ordering without promoting gelation. *NPG Asia Materials, 10*(5), 455–465.
Jiang, F., Esker, A. R., & Roman, M. (2010). Acid-catalyzed and solvolytic desulfation of H_2SO_4-hydrolyzed cellulose nanocrystals. *Langmuir: The ACS Journal of Surfaces and Colloids, 26*(23), 17919–17925.
Jiang, M., DeMass, S. N., Economy, D. R., Shackleton, T., & Kitchens, C. L. (2016). Formation of highly oriented cellulose nanocrystal films by spin coating film from aqueous suspensions. *Journal of Renewable Materials, 4*(5), 377.
Jinkins, K. R., Wang, J., Dwyer, J. H., Wang, X., & Arnold, M. S. (2021). Confined shear alignment of ultrathin films of cellulose nanocrystals. *ACS Applied Bio Materials, 4*(11), 7961–7966.
Jones, S. H., King, M. D., & Ward, A. D. (2013). Determining the unique refractive index properties of solid polystyrene aerosol using broadband Mie scattering from optically trapped beads. *Physical Chemistry Chemical Physics, 15*(47), 20735–20741.
Kang, K., & Eremin, A. (2021). Solvent-dependent morphology and anisotropic microscopic dynamics of cellulose nanocrystals under electric fields. *Physical Review E, 103*(3), Article 032606.
Kaur, B., Gur, I. S., & Bhatnagar, H. L. (1987). Thermal degradation studies of cellulose phosphates and cellulose thiophosphates. *Die Angewandte Makromolekulare Chemie, 147*(1), 157–183.
Khattab, M. M., Abdel-Hady, N. A., & Dahman, Y. (2017). 21 - Cellulose nanocomposites: Opportunities, challenges, and applications. A. K . & H.P. S (Eds.). In M. Jawaid, & S. Boufi (Eds.), *Cellulose-reinforced nanofibre composites* (pp. 483–516). Woodhead Publishing.
Kimura, F., Kimura, T., Tamura, M., Hirai, A., Ikuno, M., & Horii, F. (2005). Magnetic alignment of the chiral nematic phase of a cellulose microfibril suspension. *Langmuir: The ACS Journal of Surfaces and Colloids, 21*(5), 2034–2037.
Klockars, K. W., Tardy, B. L., Borghei, M., Tripathi, A., Greca, L. G., & Rojas, O. J. (2018). Effect of anisotropy of cellulose nanocrystal suspensions on stratification, domain structure formation, and structural colors. *Biomacromolecules, 19*(7), 2931–2943.
Kose, O., Tran, A., Lewis, L., Hamad, W. Y., & MacLachlan, M. J. (2019). Unwinding a spiral of cellulose nanocrystals for stimuli-responsive stretchable optics. *Nature Communications, 10*(1), 510.
Landry, V., Alemdar, A., & Blanchet, P. (2011). Nanocrystalline cellulose: Morphological, physical, and mechanical properties. *Forest Products Journal, 61*(2), 104–112.
Lin, N., & Dufresne, A. (2014). Surface chemistry, morphological analysis and properties of cellulose nanocrystals with gradiented sulfation degrees. *Nanoscale, 6*(10), 5384–5393.
Ling, Z., Wang, K., Liu, W., Tang, W., & Yong, Q. (2020). Tuning the cellulose nanocrystal alignments for supramolecular assembly of chiral nematic films with highly efficient UVB shielding capability. *Journal of Materials Chemistry C, 8*(25), 8493–8501.
Liu, L., Hu, Z., Sui, X., Guo, J., Cranston, E. D., & Mao, Z. (2018). Effect of counterion choice on the stability of cellulose nanocrystal pickering emulsions. *Industrial & Engineering Chemistry Research, 57*(21), 7169–7180.
Lizundia, E., Urruchi, A., Vilas, J. L., & León, L. M. (2016). Increased functional properties and thermal stability of flexible cellulose nanocrystal/ZnO films. *Carbohydrate Polymers, 136*, 250–258.
Mendoza-Galván, A., Tejeda-Galán, T., Domínguez-Gómez, A. B., Mauricio-Sánchez, R. A., Järrendahl, K., & Arwin, H. (2019). Linear birefringent films of cellulose nanocrystals produced by dip-coating. *Nanomaterials, 9*(1), 45.
Moon, R. J., Martini, A., Nairn, J., Simonsen, J., & Youngblood, J. (2011). Cellulose nanomaterials review: Structure, properties and nanocomposites. *Chemical Society Reviews, 40*(7), 3941–3994.
Natarajan, B., Emiroglu, C., Obrzut, J., Fox, D. M., Pazmino, B., Douglas, J. F., et al. (2017). Dielectric characterization of confined water in chiral cellulose nanocrystal films. *ACS Applied Materials & Interfaces, 9*(16), 14222–14231.
Natarajan, B., & Gilman, J. W. (2018a). Bioinspired Bouligand cellulose nanocrystal composites: A review of mechanical properties. *Philosophical Transactions. Series A, Mathematical, Physical, and Engineering Sciences, 376*(2112).
Natarajan, B., & Gilman, J. W. (2018b). Bioinspired Bouligand cellulose nanocrystal composites: A review of mechanical properties. *Philosophical Transactions of the Royal Society A: Mathematical, Physical and Engineering Sciences, 376*(2112), Article 20170050.
Nightingale, E., Jr (1959). Phenomenological theory of ion solvation. Effective radii of hydrated ions. *The Journal of Physical Chemistry, 63*(9), 1381–1387.
Niskanen, I., Suopajärvi, T., Liimatainen, H., Fabritius, T., Heikkilä, R., & Thungström, G. (2019). Determining the complex refractive index of cellulose nanocrystals by combination of Beer-Lambert and immersion matching methods. *Journal of Quantitative Spectroscopy and Radiative Transfer, 235*, 1–6.
Norrrahim, M. N. F., Mohd Kasim, N. A., Knight, V. F., Ujang, F. A., Janudin, N., Abdul Razak, M. A. I., et al. (2021). Nanocellulose: The next super versatile material for the military. *Materials Advances, 2*(5), 1485–1506.
Oguzlu, H., Danumah, C., & Boluk, Y. (2017). Colloidal behavior of aqueous cellulose nanocrystal suspensions. *Current Opinion in Colloid & Interface Science, 29*, 46–56.
Parit, M., Saha, P., Davis, V. A., & Jiang, Z. (2018). Transparent and homogenous cellulose nanocrystal/lignin UV-protection films. *ACS Omega, 3*(9), 10679–10691.
Park, J. H., Noh, J., Schütz, C., Salazar-Alvarez, G., Scalia, G., Bergström, L., et al. (2014). Macroscopic control of helix orientation in films dried from cholesteric liquid-crystalline cellulose nanocrystal suspensions. *Chemphyschem: A European Journal of Chemical Physics and Physical Chemistry, 15*(7), 1477–1484.
Parton, T. G., Parker, R. M., van de Kerkhof, G. T., Narkevicius, A., Haataja, J. S., Frka-Petesic, B., et al. (2022). Chiral self-assembly of cellulose nanocrystals is driven by crystallite bundles. *Nature Communications, 13*(1), 2657.
Phan-Xuan, T., Thuresson, A., Skepö, M., Labrador, A., Bordes, R., & Matic, A. (2016). Aggregation behavior of aqueous cellulose nanocrystals: The effect of inorganic salts. *Cellulose (London, England), 23*(6), 3653–3663.
Pullawan, T., Wilkinson, A. N., & Eichhorn, S. J. (2012). Influence of magnetic field alignment of cellulose whiskers on the mechanics of all-cellulose nanocomposites. *Biomacromolecules, 13*(8), 2528–2536.
Qin, X., Marchi, B. C., Meng, Z., & Keten, S. (2019). Impact resistance of nanocellulose films with bioinspired Bouligand microstructures. *Nanoscale Advances, 1*(4), 1351–1361.
Ranjbar, D., & Hatzikiriakos, S. G. (2020). Effect of ionic surfactants on the viscoelastic properties of chiral nematic cellulose nanocrystal suspensions. *Langmuir: The ACS Journal of Surfaces and Colloids, 36*(1), 293–301.
Reid, M. S., Villalobos, M., & Cranston, E. D. (2016). Cellulose nanocrystal interactions probed by thin film swelling to predict dispersibility. *Nanoscale, 8*(24), 12247–12257.
Reid, M. S., Villalobos, M., & Cranston, E. D. (2017). Benchmarking cellulose nanocrystals: from the laboratory to industrial production. *Langmuir: The ACS Journal of Surfaces and Colloids, 33*(7), 1583–1598.
Reising, A.B., Moon, R.J., & Youngblood, J.P. (2012). Effect of particle alignment on mechanical properties of neat cellulose nanocrystal films.

Reising, A. R., Moon, R., & Youngblood, J. (2012). Effect of particle alignment on mechanical properties of neat cellulose nanocrystal films. *Journal of Science & Technology for Forest Products and Processes, 2*, 32–41.
Revol, J. F., Godbout, L., Dong, X. M., Gray, D. G., Chanzy, H., & Maret, G. (1994). Chiral nematic suspensions of cellulose crystallites; phase separation and magnetic field orientation. *Liquid Crystals, 16*(1), 127–134.
Roman, M., & Gray, D. G. (2005). Parabolic focal conics in self-assembled solid films of cellulose nanocrystals. *Langmuir: The ACS Journal of Surfaces and Colloids, 21*(12), 5555–5561.
Sagou, J.-P. S., Ahualli, S., & Thomas, F. (2015). Influence of ionic strength and polyelectrolyte concentration on the electrical conductivity of suspensions of soft colloidal polysaccharides. *Journal of Colloid and Interface Science, 459*, 212–217.
Scheirs, J., Camino, G., & Tumiatti, W. (2001). Overview of water evolution during the thermal degradation of cellulose. *European Polymer Journal, 37*(5), 933–942.
Schütz, C., Agthe, M., Fall, A. B., Gordeyeva, K., Guccini, V., Salajková, M., et al. (2015). Rod packing in chiral nematic cellulose nanocrystal dispersions studied by small-angle X-ray scattering and laser diffraction. *Langmuir: the ACS journal of surfaces and colloids, 31*(23), 6507–6513.
Schütz, C., Bruckner, J. R., Honorato-Rios, C., Tosheva, Z., Anyfantakis, M., & Lagerwall, J. P. F. (2020). From equilibrium liquid crystal formation and kinetic arrest to photonic bandgap films using suspensions of cellulose nanocrystals. *Crystals, 10*(3), 199.
Shafiei-Sabet, S., Hamad, W. Y., & Hatzikiriakos, S. G. (2012). Rheology of nanocrystalline cellulose aqueous suspensions. *Langmuir: The ACS Journal of Surfaces and Colloids, 28*(49), 17124–17133.
Sirviö, J. A., Visanko, M., Heiskanen, J. P., & Liimatainen, H. (2016). UV-absorbing cellulose nanocrystals as functional reinforcing fillers in polymer nanocomposite films. *Journal of Materials Chemistry A, 4*(17), 6368–6375.
Solomon, M. J., & Spicer, P. T. (2010). Microstructural regimes of colloidal rod suspensions, gels, and glasses. *Soft Matter, 6*(7), 1391–1400.
Song, W., Lee, J. K., Gong, M. S., Heo, K., Chung, W. J., & Lee, B. Y. (2018). Cellulose nanocrystal-based colored thin films for colorimetric detection of aldehyde gases. *ACS Applied Materials & Interfaces, 10*(12), 10353–10361.
Song, Z., Ni, Y., & Cai, S. (2019). Fracture modes and hybrid toughening mechanisms in oscillated/twisted plywood structure. *Acta Biomaterialia, 91*, 284–293.
Sonker, A. K., Rathore, K., Nagarale, R. K., & Verma, V. (2018). Crosslinking of polyvinyl alcohol (PVA) and effect of crosslinker shape (Aliphatic and Aromatic) thereof. *Journal of Polymers and the Environment, 26*, 1782–1794.
Sonker, A. K., Tiwari, N., Nagarale, R. K., & Verma, V. (2016). Synergistic effect of cellulose nanowhiskers reinforcement and dicarboxylic acids crosslinking towards polyvinyl alcohol properties. *Journal of Polymer Science Part a-Polymer Chemistry, 54*(16), 2515–2525.
Sørensen, B. E. (2012). A revised Michel-Lévy interference colour chart based on first-principles calculations. *European Journal of Mineralogy, 25*(1), 5–10.
Sugiyama, J., Chanzy, H., & Maret, G. (1992). Orientation of cellulose microcrystals by strong magnetic fields. *Macromolecules, 25*(16), 4232–4234.
Tabuteau, H., Coussot, P., & Bruyn, J. R. (2007). Drag force on a sphere in steady motion through a yield-stress fluid. *Journal of Rheology, 51*(1), 125–137.
Tanaka, H., Meunier, J., & Bonn, D. (2004). Nonergodic states of charged colloidal suspensions: Repulsive and attractive glasses and gels. *Physical Review E, 69*(3), Article 031404.
Tran, A., Hamad, W. Y., & MacLachlan, M. J. (2018). Tactoid annealing improves order in self-assembled cellulose nanocrystal films with chiral nematic structures. *Langmuir: The ACS Journal of Surfaces and Colloids, 34*(2), 646–652.
Vanderfleet, O. M., Reid, M. S., Bras, J., Heux, L., Godoy-Vargas, J., Panga, M. K. R., et al. (2019). Insight into thermal stability of cellulose nanocrystals from new hydrolysis methods with acid blends. *Cellulose (London, England), 26*(1), 507–528.
Volkov, A. G., Paula, S., & Deamer, D. W. (1997). Two mechanisms of permeation of small neutral molecules and hydrated ions across phospholipid bilayers. *Bioelectrochemistry and Bioenergetics, 42*(2), 153–160.
Vollick, B., Kuo, P. Y., Alizadehgiashi, M., Yan, N., & Kumacheva, E. (2017). From structure to properties of composite films derived from cellulose nanocrystals. *ACS Omega, 2*(9), 5928–5934.
Wang, H., Shao, R., Meng, X., He, Y., Shi, Z., Guo, Z., et al. (2022). Programmable birefringent patterns from modulating the localized orientation of cellulose nanocrystals. *ACS Applied Materials & Interfaces, 14*(31), 36277–36286.
Wang, P. X., Hamad, W. Y., & MacLachlan, M. J. (2016). Structure and transformation of tactoids in cellulose nanocrystal suspensions. *Nature Communications, 7*(1), 11515.
Wojno, S., Fazilati, M., Nypelö, T., Westman, G., & Kádár, R. (2022). Phase transitions of cellulose nanocrystal suspensions from nonlinear oscillatory shear. *Cellulose (London, England), 29*(7), 3655–3673.
Xu, Y. T., Walters, C. M., D'Acierno, F., Hamad, W. Y., Michal, C. A., & MacLachlan, M. J. (2022). Cellulose nanocrystal chiral nematic composites with wet mechanical adaptability. *Chemistry of Materials, 34*(10), 4311–4319.
Xu, Y., Atrens, A., & Stokes, J. R. (2020). A review of nanocrystalline cellulose suspensions: Rheology, liquid crystal ordering and colloidal phase behaviour. *Advances in Colloid and Interface Science, 275*, Article 102076.
Xu, Y., Atrens, A. D., & Stokes, J. R. (2018). Liquid, gel and soft glass" phase transitions and rheology of nanocrystalline cellulose suspensions as a function of concentration and salinity. *Soft matter, 14*(10), 1953–1963.
Yin, S., Yang, W., Kwon, J., Wat, A., Meyers, M. A., & Ritchie, R. O. (2019). Hyperelastic phase-field fracture mechanics modeling of the toughening induced by Bouligand structures in natural materials. *Journal of the Mechanics and Physics of Solids, 131*, 204–220.
Zhao, G., Huang, Y., Mei, C., Zhai, S., Xuan, Y., Liu, Z., et al. (2021). Chiral nematic coatings based on cellulose nanocrystals as a multiplexing platform for humidity sensing and dual anticounterfeiting. *Small (Weinheim an der Bergstrasse, Germany), 17*(50), Article 2103936.
Zhao, T. H., Parker, R. M., Williams, C. A., Lim, K. T. P., Frka-Petesic, B., & Vignolini, S. (2019). Printing of responsive photonic cellulose nanocrystal microfilm arrays. *Advanced Functional Materials, 29*(21), Article 1804531.